TU Delft

Delft University of Technology

Document Version
Final published version

Citation (APA)
Shen, Q., van Dijk, N., Brück, E., & Li, L. (2025). Exploring Zero Thermal Expansion in Magnetocaloric Materials. *Advanced Engineering Materials*, *27*(20), Article 2500833. https://doi.org/10.1002/adem.202500833

Important note
To cite this publication, please use the final published version (if applicable).
Please check the document version above.

Copyright
In case the licence states “Dutch Copyright Act (Article 25fa)”, this publication was made available Green Open Access via the TU Delft Institutional Repository pursuant to Dutch Copyright Act (Article 25fa, the Taverne amendment). This provision does not affect copyright ownership.
Unless copyright is transferred by contract or statute, it remains with the copyright holder.

Sharing and reuse
Other than for strictly personal use, it is not permitted to download, forward or distribute the text or part of it, without the consent of the author(s) and/or copyright holder(s), unless the work is under an open content license such as Creative Commons.

Takedown policy
Please contact us and provide details if you believe this document breaches copyrights.
We will remove access to the work immediately and investigate your claim.

This work is downloaded from Delft University of Technology.

Green Open Access added to TU Delft Institutional Repository
as part of the Taverne amendment.

More information about this copyright law amendment
can be found at https://www.openaccess.nl.

Otherwise as indicated in the copyright section:
the publisher is the copyright holder of this work and the
author uses the Dutch legislation to make this work public.

Green Open Access added to TU Delft Institutional Repository
as part of the Taverne amendment.

More information about this copyright law amendment
can be found at https://www.openaccess.nl.

Otherwise as indicated in the copyright section:
the publisher is the copyright holder of this work and the
author uses the Dutch legislation to make this work public.

ADVANCED ENGINEERING MATERIALS
www.aem-journal.com

Check for updates

Exploring Zero Thermal Expansion in Magnetocaloric Materials

*Qi Shen, Niels van Dijk, Ekkes Brück, and Lingwei Li**

Zero thermal expansion (ZTE) materials, which maintain a constant length despite temperature variations, are highly desirable for advanced industrial applications. This review highlights recent progress in exploring ZTE behavior in Fe-based Laves phases, La–Fe–Si(Al)-based alloys, and rare-earth-based systems exhibiting the magnetocaloric effect (MCE). The abnormal lattice expansion observed in giant magnetocaloric materials, driven by magnetic interactions, provides a natural foundation for designing ZTE materials. This review offers new insights into the design and discovery of novel ZTE materials within MCE systems. Furthermore, key properties such as mechanical strength, thermal and electrical conductivity, and cycling stability are also discussed, paving the way for ZTE advancements in functional materials.

1. Introduction

Materials with precisely controlled thermal expansion are essential in modern industries, including dental components, optical mirrors, and printed electronics. In dentistry, composite materials with a tunable thermal expansion can improve the adhesion and longevity of dental restorations by better matching the thermal behavior of natural teeth. In high-precision optical applications, zero-expansion coatings on mirrors help maintain the optical performance by mitigating temperature-induced distortions. Similarly, in the electronics industry, thermally engineered materials can be tailored to match the thermal expansion of silicon substrates, thereby minimizing thermal stresses in printed circuit boards and heat sinks. Beyond these applications, magnetic materials exhibit unique thermal expansion behavior due to the interplay between magnetism and the crystal lattice. The thermal expansion of a magnetic material is primarily governed by two mechanisms: 1) conventional thermal expansion driven by lattice vibrations and 2) spontaneous magnetostriction, where the temperature-dependent magnetic moment induces volume changes via the magnetoelastic coupling. By strategically combining materials with negative thermal expansion (NTE) and positive thermal expansion (PTE), one can achieve zero thermal expansion (ZTE), enabling the development of dimensionally stable materials for advanced engineering applications. A well-known magnetic ZTE material is the Invar alloy $Fe_{65}Ni_{35}$, which has been in use since its discovery by Guillaume in 1897, a breakthrough that earned him the Nobel Prize.[1] This alloy exhibits a nearly "invariant" thermal expansion, making it widely applicable in various industrial products. The term "Invar" has become synonymous with an anomalously low thermal expansion. The Invar effect arises from a magnetovolume transition (MVE) between the larger-volume ferromagnetic state and the smaller-volume paramagnetic state.[2] Extended X-ray absorption fine structure (EXAFS) spectroscopy at the Fe and Ni *K*-edges reveals that the first nearest-neighbor shells around Fe exhibit a negligible thermal expansion, providing insight into the microscopic origins of this phenomenon.[3]

The magnetocaloric effect (MCE) refers to the thermal response of a material's lattice upon the application or removal of a magnetic field and can be characterized by the magnetic entropy change and the adiabatic temperature change.[4–8] From the perspective of energy efficiency and environmental sustainability, a wide range of magnetocaloric materials have been identified, and the underlying mechanisms responsible for their giant magnetocaloric effect have extensively been studied in various material systems such as the well-known $La(Fe, Si)_{13}$,[9–12] $(Mn, Fe)_2(P, Si)$[13–15] systems, and the rare-earth-based alloys.[16–20] In itinerant-electron systems, a large change in magnetization and in magnetic entropy is generally correlated with a significant volume change, except in cases where magnetic materials primarily undergo alterations in the ratio of the lattice parameters, as observed in Mn–Fe–P–Si alloys.[21] Several magnetocaloric materials, including FeRh[22] and $Gd_5Si_2Ge_2$,[23] undergo a significant volume expansion (0.5%–1%) during magnetoelastic or magnetostructural transitions at the magnetic phase transition. In contrast, materials such as La–Fe–Si and Fe_2(Hf, Ta) Laves alloys exhibit a substantial volume contraction (≈1%–2%) at the magnetoelastic transition.[24,25] The tunable magnetoelastic transition makes the La–Fe–Si and Fe_2(Hf, Ta) systems promising candidates for ZTE applications. Therefore, this review highlights these materials as representative magnetic thermal expansion systems and provides a brief review of rare-earth-based compounds with exceptional ZTE properties.

Q. Shen, L. Li
Key Laboratory of Novel Materials for Sensor of Zhejiang Province
Hangzhou Dianzi University
Hangzhou 310012, P. R. China
E-mail: lingwei@hdu.edu.cn

N. van Dijk, E. Brück
Fundamental Aspects of Materials and Energy, Faculty of Applied Sciences
Delft University of Technology
Mekelweg 15, 2629 JB Delft, The Netherlands

The ORCID identification number(s) for the author(s) of this article can be found under https://doi.org/10.1002/adem.202500833.

DOI: 10.1002/adem.202500833

 © 2025 Wiley-VCH GmbH

2. The Characterization of ZTE Materials

Two key parameters must be considered when evaluating the NTE performance of materials. The first is the temperature range ΔT over which the NTE occurs. Different applications require materials to maintain thermal stability within specific limits. For instance, high-precision satellite components must function reliably between −75 and 135 °C, whereas human tooth enamel operates at ≈37 °C. A wide ΔT provides more possibilities for applications. The second is the magnitude of the thermal expansion given by α_v. The volume coefficient of thermal expansion (CTE) α_v can be defined as follows

$$\alpha_v = \frac{V_1 - V_0}{V_0(T_1 - T_0)} \tag{1}$$

$$\alpha_l = \frac{l_1 - l_0}{l_0(T_1 - T_0)} \tag{2}$$

where α_v and α_l are volume and linear CTE, respectively. For first-order phase transitions, α_v diverges at the transition temperature. As a result, α_v and ΔT need to serve together as a universal measure of the strength of the NTE behavior. For isotropic systems, such as polycrystalline materials with fully randomly oriented crystals, the linear CTE α_l can be related to the volumetric CTE, α_v, by the equation $\alpha_l = 1/3\alpha_v$.[26] For simplicity of comparison, this relation is also used to estimate α_l for anisotropic systems in this review.[26] Materials with $|\alpha_v| < 3.0 \times 10^{-6}\,K^{-1}$ or $|\alpha_l| < 1.0 \times 10^{-6}\,K^{-1}$ are classified as exhibiting a ZTE.[26,27] The CTE and ΔT can be measured using several techniques, including X-ray diffraction (XRD), neutron powder diffraction (NPD), and dilatometry, each offering unique insights into the thermal expansion behavior. XRD and NPD determine the intrinsic lattice expansion by tracking unit-cell volume changes, where NPD provides a better penetration and sensitivity to light elements. In contrast, dilatometry measures macroscopic expansion, incorporating microstructural effects, such as porosity, grain boundaries, and texture, which likely lead to minor discrepancies with diffraction-based methods.[28]

The Debye–Gruneisen relationship allows estimation of the nonmagnetic thermal expansion curve by extrapolating the high-temperature paramagnetic phase data.[29,30] The spontaneous volume magnetostriction ω_s accompanying a second-order magnetic phase transition can be expressed as:

$$\omega_s = (V_{exp} - V_{nm})/V_{nm} \tag{3}$$

V_{exp} and V_{nm} refer to the measured experimental unit-cell volume and extrapolated nonmagnetic unit-cell volume, respectively. Since α_v represents the temperature derivative of ω_s, we obtain

$$\alpha_V = d\omega_s/dT \tag{4}$$

Although there is no direct link between α_v and the magnetic entropy change ΔS_M, a connection exists between ω_s and magnetization M, given by:[30]

$$\omega_s(T) = kCM(T)^2 \tag{5}$$

where k and C are the magnetoelastic coupling constant and the compressibility, respectively. Schematic illustrations for the calculation of the CTE and ω_s in an NTE material are given in **Figure 1**. The thermal expansion data of Invar alloy, Fe-based Laves phases, La–Fe–Si(Al)-based alloys, and rare-earth-based alloys are given in **Table 1**.

3. ZTE Materials

3.1. Fe-Based Laves Phase

3.1.1. Crystal Structure and Magnetic Properties

Laves phases (AB_2) are topologically close-packed intermetallic compounds, named after the German mineralogist and crystallographer Fritz Laves. They typically crystallize in one of three structural types: cubic $MgCu_2$, hexagonal $MgZn_2$, or hexagonal $MgNi_2$. The MCE near room temperature has been observed in Fe-based Laves phases. A notable example is the $Hf_{1-x}Ta_xFe_2$ system, which adopts the hexagonal $MgZn_2$-type structure (space group $P6_3/mmc$), as illustrated in **Figure 2**a,b. In this structure, Fe atoms occupy the 2*a* and 6*h* sites, while Hf/Ta atoms are positioned at the 4*f* site. With increasing temperature, $Hf_{1-x}Ta_xFe_2$ undergoes a transition from a ferromagnetic (FM) to an antiferromagnetic (AFM) state at the magnetoelastic transition temperature T_t, followed by a further transformation into the paramagnetic (PM) phase at the Néel temperature. A comprehensive phase diagram is provided.[25] In the FM state, the Fe magnetic moments at the 2*a* and 6*h* sites align within the *a*-*b* plane. In the AFM state, the Fe moments at the 2*a* site experience

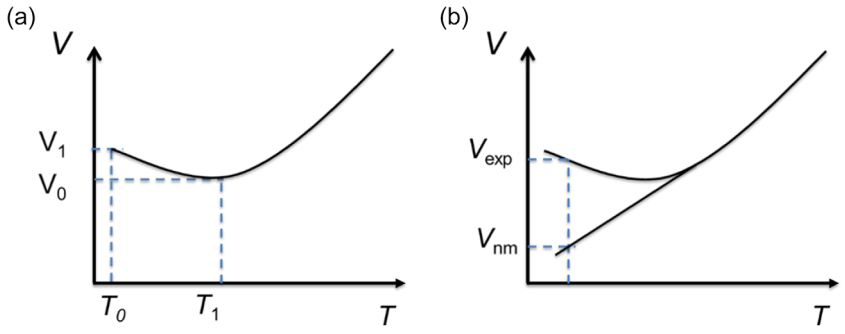

Figure 1. Schematic illustration of the calculation methodology for a) the volume coefficient of thermal expansion CTE and b) the spontaneous volume magnetostriction (ω_s) in an NTE material.

© 2025 Wiley-VCH GmbH

15272648, 0, Downloaded from https://advanced.onlinelibrary.wiley.com/doi/10.1002/adem.202500833 by Technical University Delft, Wiley Online Library on [09/09/2025]. See the Terms and Conditions (https://onlinelibrary.wiley.com/terms-and-conditions) on Wiley Online Library for rules of use; OA articles are governed by the applicable Creative Commons License

Table 1. Linear thermal expansion data (α_l) of a series of magnetic functional materials.

Composition	CTE	T [K]	Method	Composition	CTE	T [K]	Method
$Fe_{65}Ni_{35}$[1]	1.5	193–373	Dilat.	Fe_2Zr[44]	−34.0	93–1078	Dilat.
$Fe_{2.3}Hf$[47]	1.7[a]	418–523	SXRD[b]	**$Sc_{0.55}Ti_{0.45}Fe_2$**[43]	**0.4**[a]	**10–250**	**NPD**
$Fe_{2.5}Hf$	**0.4**[a]	**433–583**	**SXRD**	$Sc_{0.4}Ti_{0.6}Fe_2$	−9.5[a]	125–205	NPD
$Fe_{2.6}Hf$	1.9[a]	298–613	SXRD	$LaFe_{10.6}Si_{2.4}$[52]	−11.2	160–270	Dilat.
$Hf_{0.9}Ta_{0.1}Fe_2$[25]	−10.7	287–356	Dilat.	$LaFe_{11.5}Si_{1.5}$	−50	170–240	Dilat.
$Hf_{0.88}Ta_{0.12}Fe_2$	−14.4	250–337	Dilat.	$LaFe_{10.5}Co_{1.0}Si_{1.5}$	−26.1	240–350	Dilat.
$Hf_{0.87}Ta_{0.13}Fe_2$	−16.3	222–327	Dilat.	$LaFe_{5.4}Co_{3.5}Si_{3.35}$[54]	1.1	260–310	Dilat.
$Hf_{0.8}Zr_{0.1}Ta_{0.1}Fe_2$	−12	259–352	Dilat.	$LaFe_{10.6}Si_{2.4}$[70]	−14.2	150–300	XRD
$Hf_{0.7}Zr_{0.2}Ta_{0.1}Fe_2$	−12.4	240–352	Dilat.	**$LaFe_{10.6}Si_{2.4}$**	**−0.8**	**15–150**	**XRD**
$Hf_{0.87}Ta_{0.13}Fe_2$[67]	−12.6	250–360	Dilat.	$LaFe_{11.5}Si_{1.5}$	−50	150–250	XRD
$Hf_{0.87}Ta_{0.13}Fe_{2.05}$	−11.3	250–360	Dilat.	$LaFe_{11.5}Si_{1.5}$	−5.6	15–150	XRD
$Hf_{0.87}Ta_{0.13}Fe_{2.1}$	−7.4	250–360	Dilat.	**$LaFe_{11}Si_2$ hydride**[53]	**0.5**	**20–275**	**XRD**
$Hf_{0.87}Ta_{0.13}Fe_{2.2}$	−2.8	250–360	Dilat.	$LaFe_{10.8}CoSi_{1.2}$[55]	−20.3	190–350	Dilat.
$Fe_2Hf_{0.87}Ta_{0.13}Cu_{1.25}$[68]	1.7	50–293	Dilat.	$(LaFe_{10.8}CoSi_{1.2})_{85}Cu_{15}$	−17.6	240–360	Dilat.
$Fe_{2.5}Hf_{0.80}Ta_{0.20}$[48]	**0.352**	**265–350**	**Dilat.**	$(LaFe_{10.8}CoSi_{1.2})_{55}Cu_{45}$	−1.9	280–340	Dilat.
$Hf_{0.85}Ta_{0.15}Fe_2$[27]	−15.8[a]	240–290	XRD	$LaFe_{11.5}Al_{1.5}$[57]	−2.02	5–250	XRD
$Hf_{0.85}Ta_{0.15}Fe_2C_{0.01}$	**−0.8**	**85–245**	**XRD**	$LaFe_{11.5}Al_{1.5}$ (3 T)	−14.0	40–260	XRD
$Hf_{0.83}Ta_{0.17}Fe_2$[41]	−33.3[a]	237–277	XRD	$LaFe_{11.2}Al_{1.8}$[56]	−10.5	100–225	Dilat.
$Hf_{0.83}Ta_{0.17}Fe_2$ (Ribbon)	−6.3[a]	197–297	XRD	**$LaFe_{10.5}Al_{2.5}$**	**0.78**	**5–250**	**Dilat.**
$Fe_{1.88}Ni_{0.12}Hf_{0.9}Ta_{0.1}$[51]	**0.26**	**192–256**	**Dilat**	$LaFe_{10.3}Al_{2.7}$	0.36	5–250	Dilat.
$Fe_{1.86}V_{0.14}Hf_{0.9}Ta_{0.1}$	**−0.12**	**232–333**	**Dilat**	$TbCo_2$[28]	−6.62	173–231	Dilat.
$Fe_{1.88}Al_{0.12}Hf_{0.9}Ta_{0.1}$	**0.16**	**272–378**	**Dilat**	**$TbCo_{1.9}Fe_{0.1}$**	**0.48**	**123–307**	**Dilat.**
$Fe_{1.76}Co_{0.24}Hf_{0.9}Ta_{0.1}$	**−0.22**	**202–267**	**Dilat**	$Er_2Fe_{14}B$[65]	−1.2[a]	120–475	XRD
$Fe_2Hf_{0.95}Nb_{0.05}$[71]	−7.7[a]	323–398	XRD	$ErFe_{0.95}Co_{0.05}B$	0.5[a]	120–475	XRD
$Fe_2Hf_{0.9}Nb_{0.1}$	−7.2[a]	273–373	XRD	**$Er_2Fe_{14}B_{1.035}$**[61]	**0.28**	**100–550**	**Dilat.**
$Fe_2Hf_{0.875}Nb_{0.125}$	−6.0[a]	248–373	XRD	**$Er_2Fe_{14}B_{1.035}$**	**−0.27**[a]	**100–550**	**XRD**
$Fe_2Hf_{0.85}Nb_{0.15}$	−2.8[a]	173–323	XRD	$ErCo_{2.9}Fe_{0.1}$[60]	−6.5[a]	60–140	XRD
$Fe_2Hf_{0.82}Nb_{0.20}$[39]	**−0.4**[a]	**117–197**	**XRD**	$ErCo_{2.85}Fe_{0.15}$	−1.1[a]	70–170	XRD
$Fe_{1.95}Hf_{0.82}Nb_{0.20}$	**0.6**[a]	**117–197**	**XRD**	**$ErCo_{2.8}Fe_{0.2}$**	**0.9**[a]	**10–220**	**XRD**
$Hf_{0.85}Ti_{0.15}Fe_2$[38]	−8.3[a]	300–400	NPD	$ErCo_{2.75}Fe_{0.25}$	2.9[a]	10–300	XRD
$Hf_{0.6}Ti_{0.4}Fe_2$	−1.4[a]	120–295	SXRD	$HoFe_{17}$[72]	−4.3[a]	295–365	XRD
$Hf_{0.6}Ti_{0.4}Fe_2$	−2.2	120–325	Dilat.	**$HoFe_{16}Cr$**	**0.43**[a]	**13–330**	**XRD**
$Zr_{0.8}Nb_{0.2}Fe_2$[64]	1.4	3–470	NPD	Ho_2Fe_{17}[63]	−2.8[a]	3–250	XRD
$Zr_{0.7}Nb_{0.3}Fe_2$	−2.14	209–358	NPD	Ho_2Fe_{17}	6.5[a]	250–340	XRD
$Zr_{0.65}Nb_{0.35}Fe_2$[73]	**0.7**	**155–300**	**Dilat.**	**$Ho_2Fe_{16}Co$**	**0.2**[a]	**3–460**	**XRD**
$Zr_{9.75}Nb_{0.25}Fe_2Co_{0.1}$[49]	1.07	3–440	NPD	**$Ho_2Fe_{16}Co$**	**0.07**	**100–461**	**Dilat.**
$Zr_{0.8}Ta_{0.2}Fe_{1.7}Co_{0.3}$[50]	0.21	5–360	**Dilat.**	**$Ho_{0.04}Fe_{0.96}$**[62]	**0.19**	**100–335**	**Dilat.**
$Zr_{0.7}Ta_{0.3}Fe_2$[45]	**0.7**	**116–430**	**Dilat.**	$Ho_{0.04}Fe_{0.96}$	1.19	100–335	XRD

[a] If the thermal expansion is anisotropic, the value of the linear CTE (α_l) is estimated as one-third of the volumetric CTE (α_V). [b] SXRD: Synchrotron XRD and Dilat.: dilatometry. The data in bold correspond to a ZTE with $|\alpha_l| < 1.0 \times 10^{-6}\ K^{-1}$.

frustration due to their intermediate position between two antiferromagnetic planes, as revealed by neutron diffraction.[31] The magnetic structures of $Hf_{1-x}Ta_xFe_2$ are depicted in Figure 2c,d.

The magnetic entropy change for a field change of $\Delta\mu_0 H = 3$ T varies between 1 and 6 J kg^{-1} K^{-1} for the Fe_2(Hf, Ta) system, depending on the Ta content.[27,32–36] A decrease in lattice parameter a and unit cell V accompanied by the FM-AFM transition at 253 K is shown in **Figure 3**b,c. A significant adiabatic temperature change of 3.5 K ($\Delta\mu_0 H = 2$ T) has been reported for $Fe_2Hf_{0.84}Ta_{0.16}$,[34] as shown in Figure 3d. Doping with elements

© 2025 Wiley-VCH GmbH

15272648, 0, Downloaded from https://advanced.onlinelibrary.wiley.com/doi/10.1002/adem.202500833 by Technical University Delft, Wiley Online Library on [09/09/2025]. See the Terms and Conditions (https://onlinelibrary.wiley.com/terms-and-conditions) on Wiley Online Library for rules of use; OA articles are governed by the applicable Creative Commons License

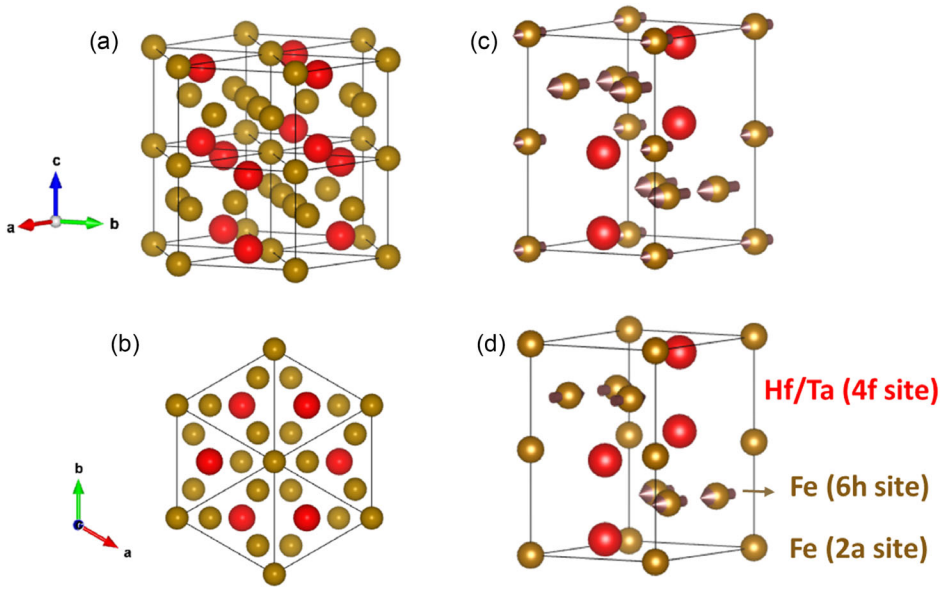

Figure 2. a,b) Unit-cell structure of the $MgZn_2$-type structure of Fe_2(Hf, Ta) Laves phase compound. Magnetic structure of Fe_2(Hf, Ta): c) ferromagnetic structure and d) antiferromagnetic structure. Fe atoms occupy the 2*a* and 6*h* sites, while Hf/Ta atoms are positioned at the 4*f* site. Reproduced under the terms of the CC BY license.[69] Copyright 2023, The Authors. Published by TU Delft.

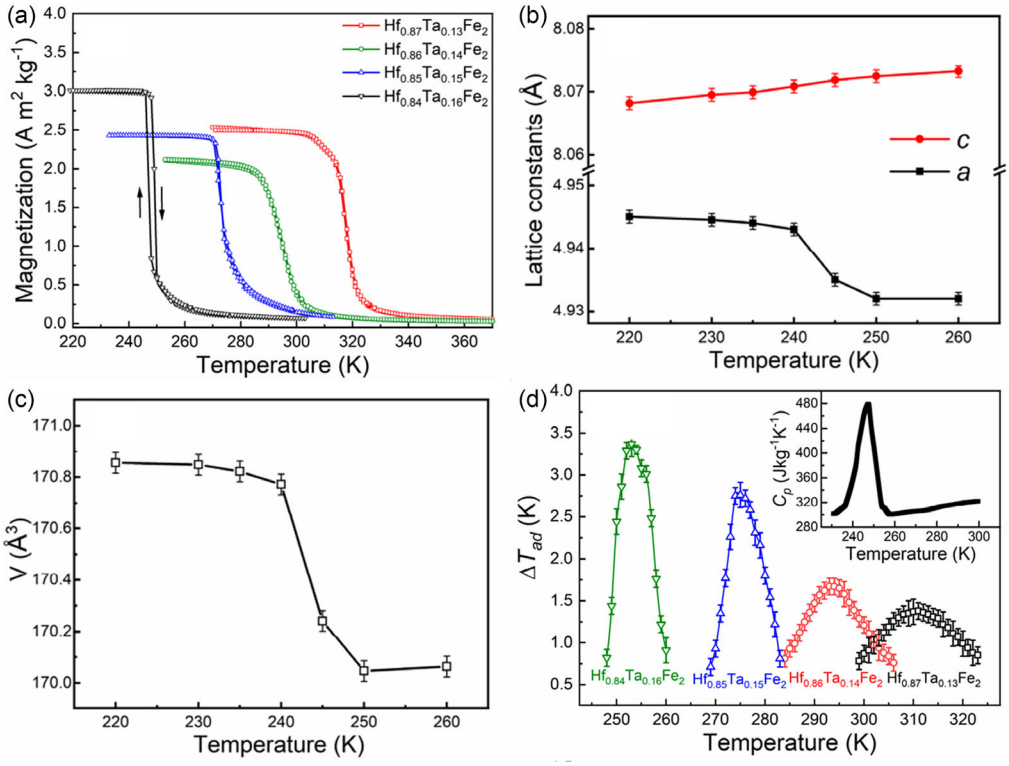

Figure 3. a) *M-T* curves for the $Hf_{1-x}Ta_xFe_2$ ($x = 0.13$, 0.14, 0.15, 0.16) alloys in a magnetic field of 0.005 T. Lattice parameters from temperature-dependent XRD data: b) Change of lattice parameters *a* and *c* as a function of temperature, and c) Temperature dependence of unit-cell volume for the $Hf_{0.84}Ta_{0.16}Fe_2$ alloy. d) Directly measured the temperature dependence of ΔT_{ad} in a magnetic field change of 1.5 T. The inset shows the specific heat capacity for the $Hf_{0.84}Ta_{0.16}Fe_2$ alloy. Reproduced under the terms of the CC BY license.[34] Copyright 2021, The Authors. Published by MDPI.

© 2025 Wiley-VCH GmbH

15272648, 0, Downloaded from https://advanced.onlinelibrary.wiley.com/doi/10.1002/adem.202500833 by Technical University Delft, Wiley Online Library on [09/09/2025]. See the Terms and Conditions (https://onlinelibrary.wiley.com/terms-and-conditions) on Wiley Online Library for rules of use; OA articles are governed by the applicable Creative Commons License

15272648, 0, Downloaded from https://advanced.onlinelibrary.wiley.com/doi/10.1002/adem.202500833 by Technical University Delft, Wiley Online Library on [09/09/2025]. See the Terms and Conditions (https://onlinelibrary.wiley.com/terms-and-conditions) on Wiley Online Library for rules of use; OA articles are governed by the applicable Creative Commons License

such as C and Co affects the magnetocaloric properties: carbon doping enhances the magnetoelastic coupling and increases ΔS_M from 1.8 J kg^{-1} K^{-1} for $Fe_2Hf_{0.85}Ta_{0.15}$ to 4.0 J kg^{-1} K^{-1} for $Fe_2Hf_{0.85}Ta_{0.15}C_{0.01}$ in a magnetic field change of 2 T;[27] Co doping reduces T_t, while maintaining a significant magnetic entropy change.[37] Additionally, a stable MCE of ≈5 J kg^{-1} K^{-1} at 7 T has been achieved in $Hf_{0.85}Ta_{0.15}Fe_2$, with an ultrawide operational temperature range of 146–320 K through hydrostatic pressure manipulation below 1 GPa.[36] The magnetocaloric effect has also been reported in Fe_2(Hf,Ti),[38] Fe_2(Hf, Nb)[39] and Fe_2(Sc, Ti)[40] alloys. Notably, $Fe_2Sc_{0.3}Ti_{0.7}$ undergoes a ferro-ferromagnetic transition where FM and canted AFM coexist below the transition temperature of 125 K. The ΔS_M values for $Fe_2Sc_{0.3}Ti_{0.7}$ are 3.4 J kg^{-1} K^{-1} at 106 K and 1.7 J kg^{-1} K^{-1} at 337 K for a magnetic field change of 5 T, corresponding to the ferro-ferromagnetic and ferro-paramagnetic transitions, respectively.[40]

3.1.2. ZTE Properties

During the FM-AFM transition, the lattice parameter a decreases, while the lattice parameter c remains constant, leading to a 0.4% reduction in the unit-cell volume for $Hf_{0.84}Ta_{0.16}Fe_2$ alloy, as shown in Figure 3d.[25] This characteristic makes the Fe_2(Hf, Ta) compounds promising candidates for NTE materials. By reducing the Ta concentration, the initially sharp volume change gradually transformed into a continuous one and shifted toward room temperature. The optimal NTE behavior is optimized at $x = 0.13$, exhibiting a linear NTE coefficient of -16.3×10^{-6} K^{-1} over a broad temperature window of 105 K (222 K−327 K).[25] A continuous magnetoelastic transition can also be achieved in $Fe_2Hf_{0.83}Ta_{0.17}$ synthesized via rapid solidification technique, which shows a linear NTE coefficient of -6.3×10^{-6} K^{-1} over a 100 K range (197 K−297 K).[41] The broadened NTE window is closely linked to the asynchronous FM ordering of the Fe moments at the 6*h* and 2*a* Fe sites,[25] derived from the Electron Spin Resonance measurements.

A similar NTE has been reported in other Fe-based Laves phase compounds, such as $Fe_2Hf_{0.80}Nb_{0.20}$ (-5×10^{-6} K^{-1}, 150–240 K),[42] $Fe_2Hf_{0.85}Ti_{0.15}$ (-8.3×10^{-6} K^{-1}, 300–400 K)[38] and $Fe_2Sc_{0.4}Ti_{0.6}$ (-9.5×10^{-6} K^{-1}, 125–205 K).[43] For $Fe_2Hf_{0.85}Ti_{0.15}$, the magnetic moments of Fe align in the *a*-*b* plane below 400 K, and their variation is responsible for the NTE over a wide temperature range of 300–400 K, as shown in **Figure 4**. The identical trends of $d\omega_s/dT$ and dM/dT confirm the strong magneto-lattice coupling in this system. A sharp magnetic transition indicates that spontaneous magnetostriction drives thermal contraction, leading to the NTE. NPD results show that the shortest in-plane Fe_{6h}–Fe_{6h} distance, as shown in Figure 4d, controls the magnetic interactions in Fe_2(Hf, Ti), making the temperature-dependent reduction of the in-plane Fe moments the key factor in the NTE. Additionally, the metallic framework-like compound $FeZr_2$ exhibits giant uniaxial NTE with $\alpha_l = -34.01 \times 10^{-6}$ K^{-1} across an extensive temperature range (93–1078 K).[44] Investigations using SXRD, NPD, neutron pair distribution functions, EXAFS, and density functional theory calculations indicate that strong Fe $3dz^2$–$3dz^2$ electron

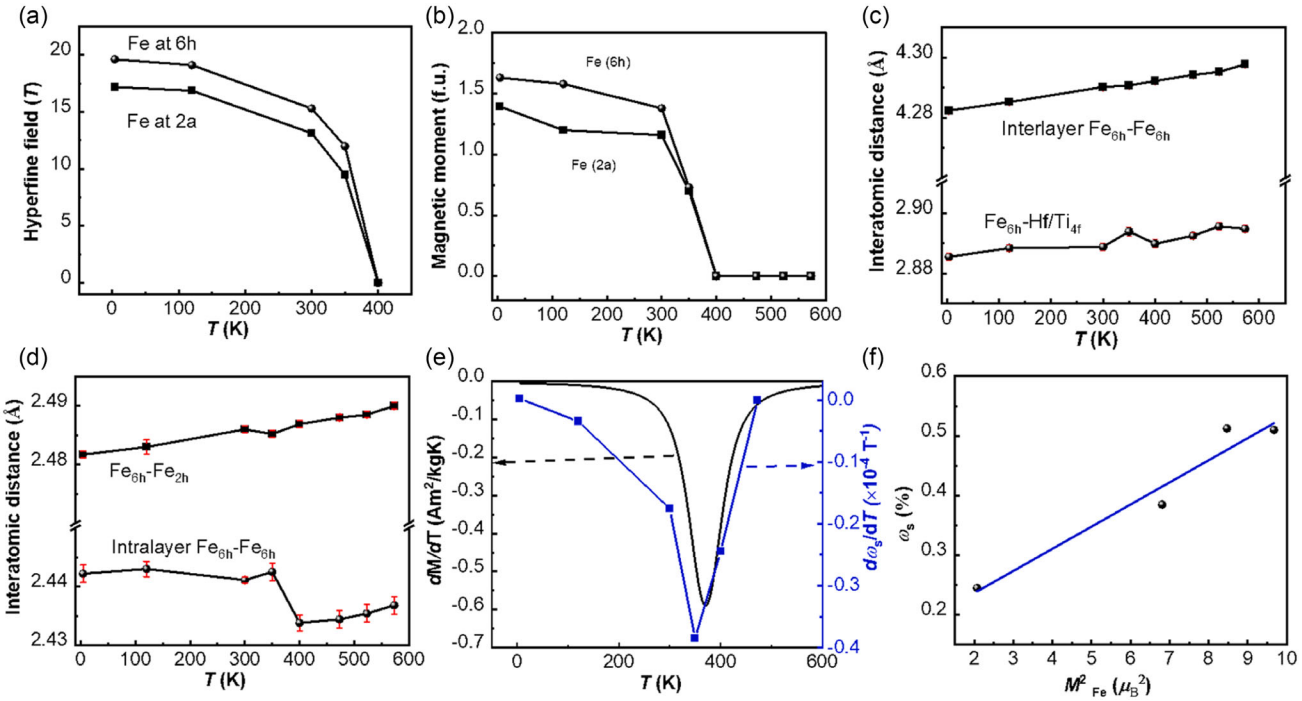

Figure 4. a) Temperature dependence of the hyperfine field of the arc-melted $Fe_2Hf_{0.85}Ta_{0.15}$ alloy, derived from Mössbauer spectroscopy. b) Temperature dependence of magnetic moment at the 2*a* and 6*h* sites of the arc-melted $Fe_2Hf_{0.85}Ta_{0.15}$ alloy derived from NPD. c,d) Interatomic distance as a function of temperature. e) $d\omega_s/dT$ and dM/dT (at a magnetic field of 1 T) as a function of temperature. f) Spontaneous volume magnetostriction ω_s as a function of the square of the Fe magnetic moment. Reproduced under the terms of the CC BY license.[38] Copyright 2021, The Authors. Published by Elsevier.

 © 2025 Wiley-VCH GmbH

interactions reinforce the Fe—Fe bond, supporting a high *c/a* ratio in the $CuAl_2$-type structure, which accommodates contraction along the *c* axis due to the strong expansion of the Fe—Zr bond. Unlike the conventional framework, NTE materials driven by low-frequency phonons, this giant uniaxial NTE arises from the coupling of a flexible, weak-bonded structure and high-frequency phonons.

Beyond the NTE, Fe-based Lave phase compounds can also show a ZTE. $Sc_{0.55}Ti_{0.45}Fe_2$ demonstrates a near-zero expansion with $\alpha_l = 0.41 \times 10^{-6}\,K^{-1}$ over 10–250 K,[43] while $Fe_2Zr_{0.7}Ta_{0.3}$ exhibits an isotropic ZTE ($\alpha_l = 0.9 \times 10^{-6}\,K^{-1}$, 10–450 K) due to its extended magnetic ordering window.[45] Neutron diffraction, Mössbauer spectroscopy, and theoretical calculations reveal that the transition from an AFM hexagonal phase to a FM cubic phase in Kagomé Fe layers plays a crucial role in this behavior. An ultrawide ZTE behavior with an average linear thermal expansion coefficient of $\alpha_l = +0.47 \times 10^{-6}\,K^{-1}$ is observed in $Zr_{0.65}Nb_{0.35}Fe_{2.15}$, spanning a broad temperature range of 4–425 K (**Figure 5**b).[46] This ZTE is attributed to interplanar ferromagnetic ordering, which induces strong spontaneous magnetic compensation for the intrinsic lattice expansion. Notably, trace Fe doping at the 8*a* crystallographic sites (Figure 5d), as confirmed by NPD and Mössbauer spectroscopy, significantly enhances the interplanar exchange interactions and raises the Curie temperature. This enables tunable thermal expansion behavior through targeted compositional control.

Off-stoichiometry has proven to be an effective strategy for achieving ZTE in Fe-based Laves phase compounds. In particular, introducing excess Fe atoms into the Fe_2Hf system leads to notable ZTE behavior. For instance, $Fe_{2.5}Hf$ exhibits a broad high-temperature ZTE range ($\alpha_l = 0.42 \times 10^{-6}\,K^{-1}$, 433−583 K), where the extra Fe atoms occupy 4*f* sites, as confirmed by NPD and Mössbauer spectroscopy.[47] The ZTE mechanism in $HfFe_{2.5}$ is closely linked to MVE, with ω_s effectively counteracting the normal thermal expansion. Moreover, the increased number of magnetic exchange interaction paths due to off-stoichiometry further tunes the lattice response, offering a promising route to designing high-temperature ZTE materials. This strategy is further supported by observations in other off-stoichiometric systems. In as-cast $Hf_{0.80}Ta_{0.20}Fe_{2.5}$, ZTE is observed in the temperature range of 265–350 K, with $\alpha_l = 0.352 \times 10^{-6}\,K^{-1}$, where the formation of a Fe-rich phase contributes to the overall thermal expansion behavior.[48] Similarly, the presence of Fe vacancies can also induce ZTE, as demonstrated in $Fe_{1.95}Hf_{0.8}Nb_{0.2}$ ($\alpha_l = -0.4 \times 10^{-6}\,K^{-1}$, 117–197 K). In this case, fine-tuning the coexistence of AFM and FM phases allows precise control over thermal expansion.[39]

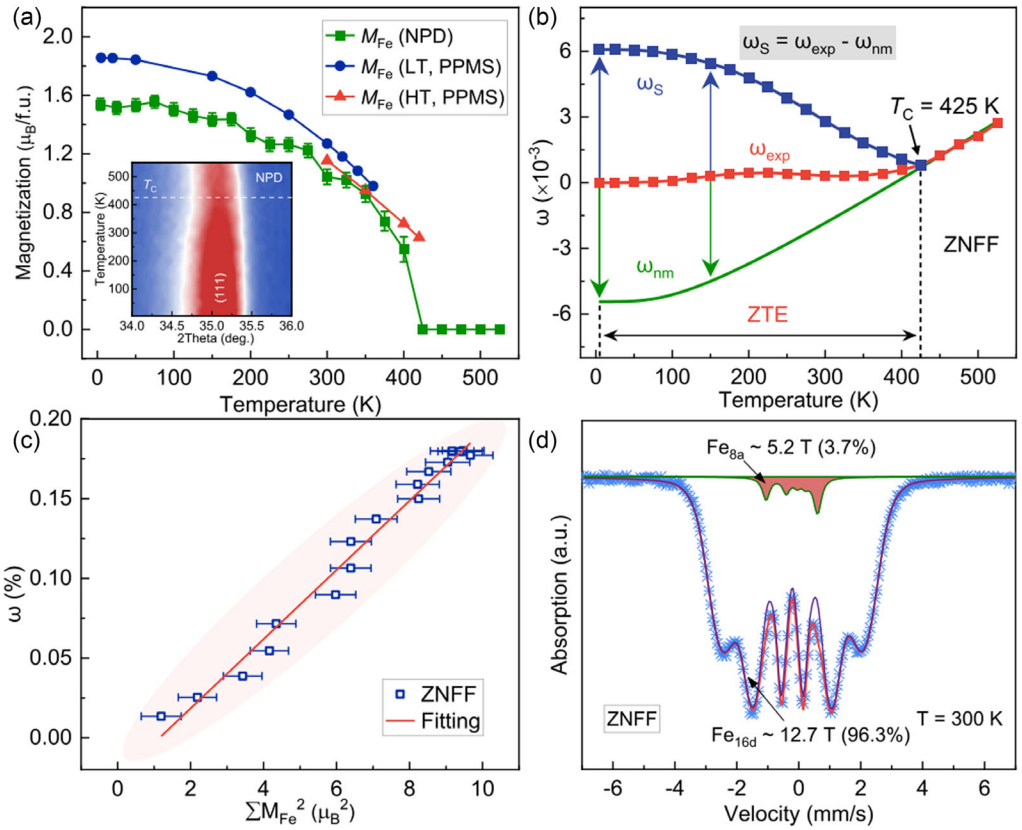

Figure 5. a) Temperature dependence of Fe magnetic moments of ZNFF ($Zr_{0.65}Nb_{0.35}Fe_{2.15}$) measured by NPD and PPMS. The inset shows a contour plot of the ZNFF peak (111) by NPD. b) Proposed process that magnetic ordering contributes to tuning ZTE for ZNFF. c) Positive correlation between the magnetic moment of the Fe lattice (|Σ*M*Fe|) and the contribution of the magnetic order to the unit-cell volume (ω_S); d) ^{57}Fe Mössbauer spectrum of ZNFF measured at 300 K. Reproduced with permission.[46] Copyright 2023, American Chemical Society.

© 2025 Wiley-VCH GmbH

15272648, 0, Downloaded from https://advanced.onlinelibrary.wiley.com/doi/10.1002/adem.202500833 by Technical University Delft, Wiley Online Library on [09/09/2025]. See the Terms and Conditions (https://onlinelibrary.wiley.com/terms-and-conditions) on Wiley Online Library for rules of use; OA articles are governed by the applicable Creative Commons License

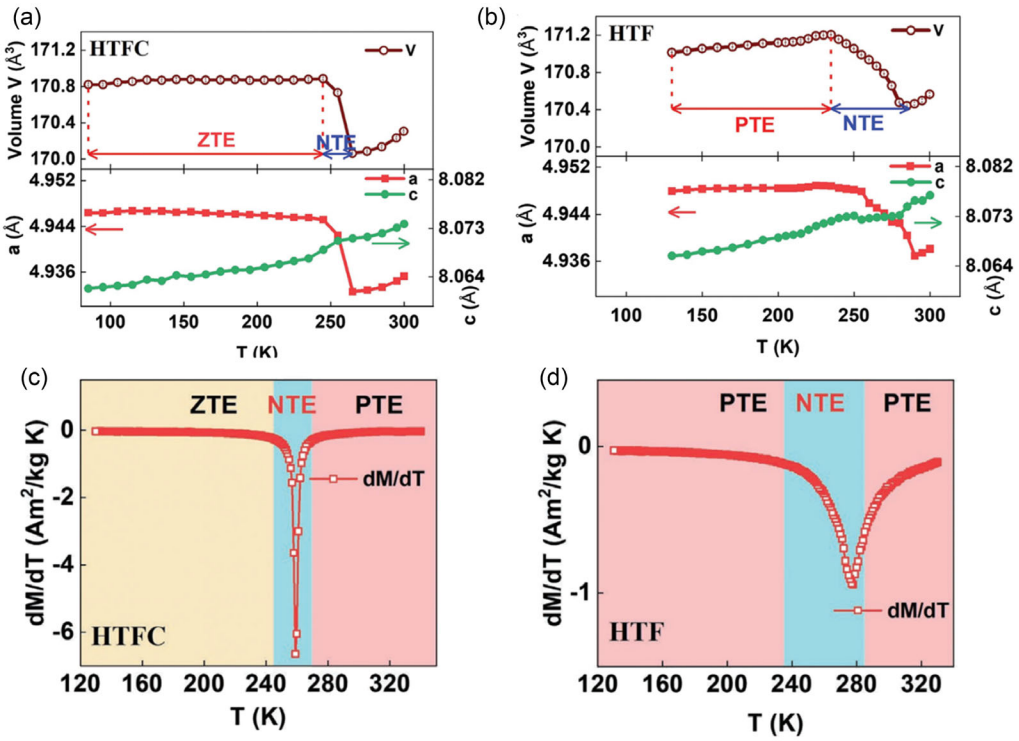

Figure 6. Temperature dependence of lattice constants *a* and *c* and the cell volume *V* in a) HTFC ($Hf_{0.85}Ta_{0.15}Fe_2C_{0.01}$) and b) HTF ($Hf_{0.85}Ta_{0.15}Fe_2$) alloys, respectively. Temperature dependence of the first reciprocal of magnetization and magnetoelastic coupling in c) HTFC and d) HTF magnets. The first derivative of magnetization *dM*/*dT* under a 1 T magnetic field, showing stronger coupling between magnetization and lattice after the addition of interstitial Carbon. Reproduced with permission.[27] Copyright 2023, John Wiley & Sons, Inc.

In addition to off-stoichiometry, elemental doping offers another effective means of realizing ZTE in Fe-based Laves phases. Carbon doping in $Hf_{0.85}Ta_{0.15}Fe_2C_{0.01}$ leads to a low α_l of $-2.2 \times 10^{-6}\,K^{-1}$ over the 85–245 K temperature range, as shown in **Figure 6**.[27] The trace interstitial carbon enhances magnetoelastic coupling in the stabilized ferromagnetic state, effectively suppressing PTE and enabling high-performance ZTE. Doping with transition metals has also led to significant advances. The pyrochlore-structured $Zr_{0.75}Nb_{0.25}Fe_2Co_{0.1}$[49] achieves a low linear CTE of $1.07 \times 10^{-6}\,K^{-1}$ over the wide temperature range of 3–440 K. Here, local compositional fluctuations of Fe and Co modulate interplanar ferromagnetic ordering, gradually counteracting normal phonon-driven expansion upon heating. Beyond thermal performance, this alloy also exhibits excellent corrosion resistance in both acidic and alkaline environments, highlighting its practical potential. Another high-performance ZTE alloy $Zr_{0.8}Ta_{0.2}Fe_{1.7}Co_{0.3}$ exhibits an isotropic ZTE behavior ($\alpha_l = 0.21 \times 10^{-6}\,K^{-1}$) over a wide 5–360 K temperature range.[50] This material also shows superior corrosion resistance in seawater-like environments, surpassing both classic and stainless Invar alloys. Its impressive cyclic thermal stability arises from its cubic symmetry, tunable magnetic ordering, and the formation of a self-passivating surface layer rich in Ta and Zr.

In parallel, room-temperature ZTE has been successfully achieved in $Fe_2Hf_{0.9}Ta_{0.1}$ alloys doped with Co, Ni, V, or Al.[51] These dopants influence the formation of different Laves phase structures: Co and Ni promote a mixture of C14 and C15 phases, while Al and V lead to the coexistence of two C14 phases. The thermal expansion behavior in these systems is governed by the atomic size ratio (r_A/r_B) and the electron concentration (*e*/*a*). Elements like V and Al, with smaller (r_A/r_B) and lower *e*/*a* values, favor the C14 phase, while higher values promote stabilization of the C15 structure. The coexistence of phases with opposing thermal expansion responses allows for effective compensation of lattice changes, resulting in significant ZTE.

3.2. La–Fe–Si (Al)-Based Alloys

3.2.1. Crystal Structure and Magnetic Properties

La–Fe–Si(Al)-based alloys crystallize in a cubic $NaZn_{13}$-type structure with space group *Fm*-3*c*, as shown in **Figure 7**a.[12] In the structure, La atoms occupy the 8*a* site, while Fe atoms are distributed between the 8*b* and 96*i* sites. Al or Si randomly substitutes for Fe at the 96*i* site. Pure $LaFe_{13}$ does not exist due to the positive formation enthalpy between La and Fe atoms, but $LaFe_{13-x}Si_x$ compounds with Si content ranging from $x = 1.2$ to 2.4 were successfully synthesized.[10,24] $LaFe_{11.4}Si_{1.6}$ exhibits a large $-\Delta S_M$ of 19.4 J kg^{-1} K^{-1} around 213 K under a magnetic field change of 5 T, driven by a field-induced itinerant-electron metamagnetic transition.[10]

Co substitution for Fe or interstitial H doping modifies the exchange coupling between magnetic elements, enabling phase transition tuning across a broad temperature range, while

© 2025 Wiley-VCH GmbH

15272648, 0, Downloaded from https://advanced.onlinelibrary.wiley.com/doi/10.1002/adem.202500833 by Technical University Delft, Wiley Online Library on [09/09/2025]. See the Terms and Conditions (https://onlinelibrary.wiley.com/terms-and-conditions) on Wiley Online Library for rules of use; OA articles are governed by the applicable Creative Commons License

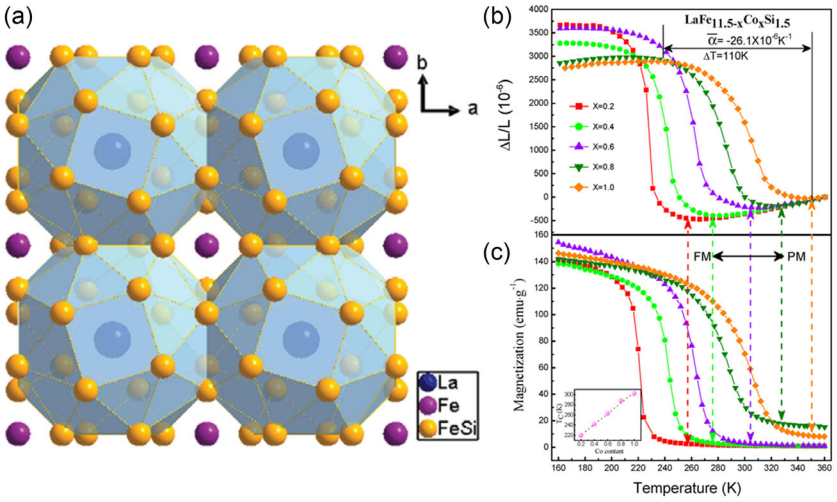

Figure 7. a) Crystal structure of LaFeSi alloys. Reprinted with permission.[12] Copyright 2018, Elsevier. b) Temperature dependence of linear thermal expansions $\Delta L/L$ and c) temperature dependence of magnetizations for $LaFe_{11.5-x}Co_xSi_{1.5}$ ($x = 0.2$, 0.4, 0.6, 0.8, and 1.0). (Inset) Curie temperatures of $LaFe_{11.5-x}Co_xSi_{1.5}$ ($x = 0.2$, 0.4, 0.6, 0.8, and 1.0). Reproduced with permission.[52] Copyright 2013, American Chemical Society.

preserving a large MCE.[9,24] Hydrogen doping shifts the first-order magnetic transition to higher temperatures, yielding $-\Delta S_M \approx 20\ J\ kg^{-1}\ K^{-1}$ and an adiabatic temperature change of 6 K for a 2 T field change over 195–336 K in $La(Fe_{0.88}Si_{0.12})_{13}H_y$ compounds.[9] The strong MCE correlates with a negative lattice expansion across the phase transition, as shown by temperature-dependent lattice parameters in $LaFe_{11.5-x}Co_xSi_{1.5}$ ($x = 0.2-1.0$) compounds,[52] as shown in Figure 7b. A detailed review on the MCE in LaFeSi-based alloys can be found.[24]

3.2.2. ZTE Properties

Huang et al. first reported a giant NTE in $La(Fe, Si, Co)_{13}$ compounds.[52] In $LaFe_{11.5-x}Co_xSi_{1.5}$, increasing Co content expands the NTE temperature window, with $LaFe_{10.5}Co_{1.0}Si_{1.5}$ exhibiting a large linear NTE coefficient of $-26.1 \times 10^{-6}\ K^{-1}$ over 240–350 K. Interstitial hydrogen shifts the NTE range in $LaFe_{11.0}Si_{2.0}$ from 175–250 K to 275–350 K and its hydride show broad ZTE behavior, ($\alpha_l = 0.5 \times 10^{-6}\ K^{-1}$, 20–275 K).[53] Yu et al. reported a near-isotropic ZTE ($\alpha_l = 1.10 \times 10^{-6}\ K^{-1}$, 260–310 K) in $LaFe_{54}Co_{3.5}Si_{3.35}$ alloy, which also demonstrates exceptional toughness (277.8 Jcm^{-3}).[54] This is attributed to a precise chemical regulation, involving phase structure (L/α phase), chemical composition, and heterogeneous microstructure, as revealed by SXRD, Electron Back-Scattering patterns, 3D Atom Probe Tomography, and high-resolution transmission electron microscopy analysis, as shown in **Figure 8**. Cu doping in $LaFe_{10.8}CoSi_{1.2}$ enhances the compression strength from 70 MPa to 645 MPa and improves plasticity.[55] The $(LaFe_{10.8}CoSi_{1.2})_{55}Cu_{45}$ alloy achieves a low linear CTE of $-1.9 \times 10^{-6}\ K^{-1}$ over a 280−340 K temperature range with high mechanical reliability after 10^4 thermal cycles. Cu addition promotes the formation of the $LaCu_2$ phase, which is semi-coherent with the La(Fe, Co, Si)$_{13}$ matrix, and the LaCuSi phase, strengthening the structure through semi-coherent interfaces and stacking faults.

Li et al. reported that $LaFe_{13-x}Al_x$ ($x = 1.8$) exhibits a linear CTE of $10.47 \times 10^{-6}\ K^{-1}$ between 100 and 225 K.[56] An increasing Al content broadens the ZTE range to 5–250 K with $x = 2.5$ ($\alpha_l = 0.78 \times 10^{-6}\ K^{-1}$) and $x = 2.7$ ($\alpha_l = 0.36 \times 10^{-6}\ K^{-1}$). Song et al. observed a slight NTE in $LaFe_{11.5}Al_{1.5}$ ($\alpha_l = -2.02 \times 10^{-6}\ K^{-1}$, 5−250 K) without a magnetic field, while applying 3 T induced a strong NTE ($\alpha_l = -14.01 \times 10^{-6}\ K^{-1}$, 40−260 K).[57] This enhancement is attributed to a ferromagnetic strengthening via spin-moment rotation in the canted structure, as revealed by neutron powder diffraction and small-angle neutron scattering.

3.3. Rare-Earth-Based Alloys

3.3.1. Crystal Structure and Magnetic Properties

Rare-earth compounds such as RCo_2 (R = Pr, Nd, Sm, Gd, Tb, Dy, Ho, Er) are promising for the MCE due to their large localized magnetic moments. Detailed reviews on the MCE in rare-earth compounds are available.[18,20,58] Er(Ho)Co_2-based compounds are promising for hydrogen liquefaction (20–77 K), exhibiting a $\Delta S_M \approx -25\ J\ kg^{-1}\ K^{-1}$ and $\Delta T_{ad} \approx 4$ K under a 5 T field change.[17] Another notable RCo_2 alloy is $TbCo_2$, which undergoes a paramagnetic-to-ferrimagnetic (PM-FIM) transition at $T_C = 231$ K. The Co magnetic state depends on the 4*f*-3*d* exchange interactions and lattice parameters. Fe substitution at the Co site shifts T_C toward room temperature while maintaining a table-like $\Delta S_M \approx 4\ J\ kg^{-1}\ K^{-1}$ over 210–320 K under a field change of 5 T.[59] **Figure 9** shows the magnetic structure for the $TbCo_{1.9}Fe_{0.1}$ alloy obtained from NPD.[28] The magnetic moments of the Co/Fe atoms at the 9*e* and 3*b* sites align antiparallel to those of the Tb atoms at the 6*c* site. At $T_C = 307$ K, the ferrimagnetic rhombohedral structure (R-3m) transforms to the paramagnetic cubic structure (Fd-3m). Since the lattice parameter c exhibits an almost linear decrease with the Tb magnetic moment, a rapid decline

© 2025 Wiley-VCH GmbH

15272648, 0, Downloaded from https://advanced.onlinelibrary.wiley.com/doi/10.1002/adem.202500833 by Technical University Delft, Wiley Online Library on [09/09/2025]. See the Terms and Conditions (https://onlinelibrary.wiley.com/terms-and-conditions) on Wiley Online Library for rules of use; OA articles are governed by the applicable Creative Commons License

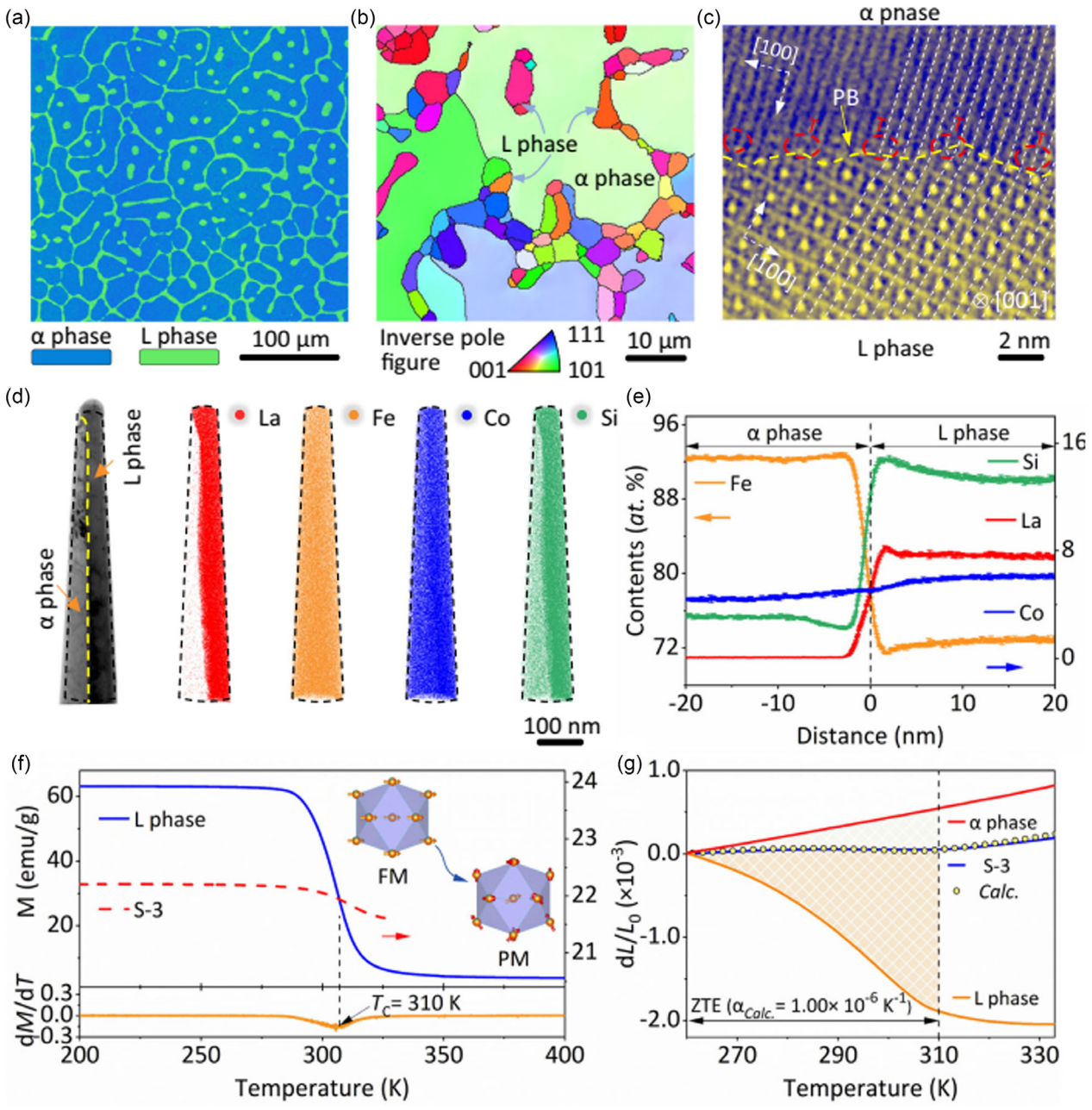

Figure 8. a) Electro-probe microanalyzer image of the S-3 ($LaFe_{0.939x}Co_{0.061x}Si_{0.0583x}$ with $x = 57.5$) alloy. b) Electron back-scattered diffraction inverse pole map of the S-3 alloy at high scales. c) High-angle annular dark-field scanning TEM image of the corresponding phase interface along the $[001]_L$ zone axis. d) Atom maps reconstructed using 3D atom probe tomography marked in the nanoprobe with the phase interface. e) 1D concentration profile of the elemental distributions. f) Field-cooling magnetization at a magnetic field of L-phase ($LaFe_{10.30}Co_{0.83}Si_{1.87}$, 0.1 T) and S-3 (0.05 T), respectively. Insert the magnetic structure model from FM to PM. g) The dilatometer thermal expansion of S-3, L-phase, $Fe_{92.42}Co_{4.34}Si_{3.07}$ (α phase) alloys. The calculated S-3 ZTE (empty circle point line) derived from L-phase and α-phase thermal expansions is consistent with the experimental data. Reproduced under the terms of the CC BY license.[61] Copyright 2024, The Authors. Published by Springer Nature.

in the Tb moment induces NTE, while a relatively slow decrease gives rise to ZTE. Notably, $TbCo_{1.9}Fe_{0.1}$ exhibits a negligible coefficient of thermal expansion ($\alpha_l = 0.48 \times 10^{-6}\,K^{-1}$) over a broad temperature range (123−307 K), further enhancing its suitability for advanced thermal management applications.

3.3.2. ZTE Properties

For rare-earth-based alloys, their complex magnetic structure and exchange coupling may provide new insights into the design and development of novel magnets with high-performance ZTE over a broad temperature range. $ErCo_{2.8}Fe_{0.2}$ magnet exhibits ZTE

© 2025 Wiley-VCH GmbH

15272648, 0, Downloaded from https://advanced.onlinelibrary.wiley.com/doi/10.1002/adem.202500833 by Technical University Delft, Wiley Online Library on [09/09/2025]. See the Terms and Conditions (https://onlinelibrary.wiley.com/terms-and-conditions) on Wiley Online Library for rules of use; OA articles are governed by the applicable Creative Commons License

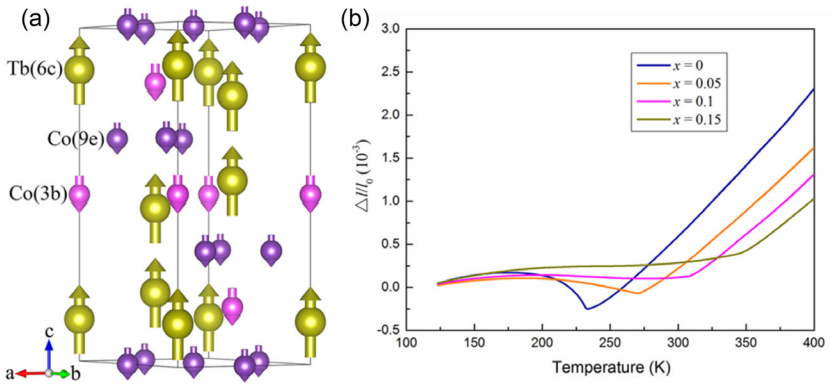

Figure 9. a) Crystal and magnetic structure of the $TbCo_{1.9}Fe_{0.1}$ intermetallic compounds at 10 K by NPD. b) Temperature dependence of linear thermal expansion ($\Delta l/l_0$) of $Tb(Co_{2-x}Fe_x)$ determined by a thermo-dilatometer. Reproduced with permission.[28] Copyright 2018, American Chemical Society.

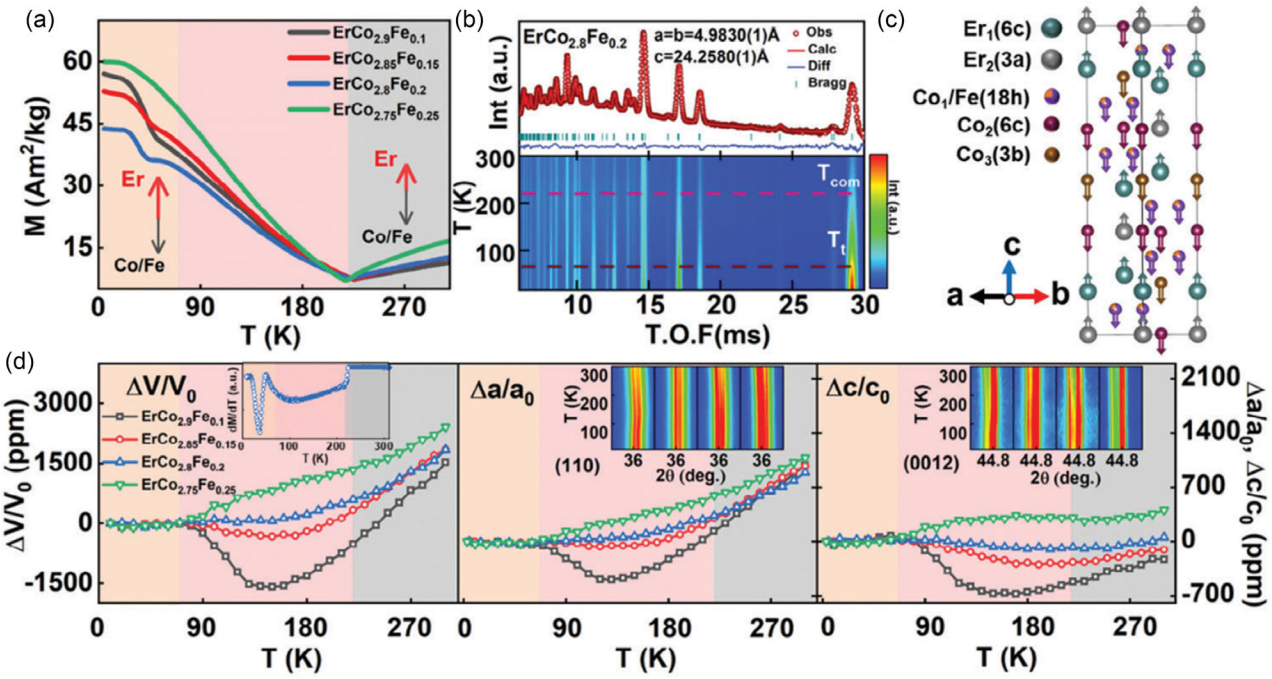

Figure 10. a) Temperature dependence of magnetization under a magnetic field of 5 T. b,c) Refined NPD pattern at 300 K. d) Tunable lattice thermal expansion ranging from NTE to ZTE and to PTE via Fe substitution; the lattice thermal expansion behavior is separated into three distinct regions marked in different colors. Reproduced with permission.[60] Copyright 2023, John Wiley & Sons, Inc.

with a negligible CTE ($\alpha_l = 0.9 \times 10^{-6}\,K^{-1}$, 10–220 K),[60] as shown in **Figure 10**. The sublattice MVE in Er1 and Er2 atoms, responsible for the ZTE and tunable physical properties, was elucidated through NPD and in situ transmission electron microscopy (TEM) magnetic domain observations. A dual-phase Er-Fe-B alloy achieves an axial ZTE ($\alpha_l = 0.28 \times 10^{-6}\,K^{-1}$, 100–550 K) combined with a high strength, stiffness, and robust thermal shock resistance,[61] attributed to a distinctive "plum pudding" structure—an $Er_2Fe_{14}B$ matrix (NTE, pudding) embedded with α-Fe (PTE, plum). The low-cost $Ho_{0.04}Fe_{0.96}$ alloy demonstrates an axial ZTE ($0.19 \times 10^{-6}\,K^{-1}$, 100–335 K).[62] Unlike the brittle intermetallic ZTE compounds, this dual-phase alloy maintains a good strength-plasticity balance, as its eutectic lamellar structure suppresses shear micro-cracks in the brittle H phase via the soft α phase after 12% deformation.

Adjusting the Co content in $Ho_2Fe_{17-x}Co_x$ tunes thermal expansion, with $Ho_2Fe_{16}Co$ achieving a record-wide ZTE range ($0.07 \times 10^{-6}\,K^{-1}$, 3–461 K) comparable to the Invar alloy,[63] as shown in **Figure 11**a,b. This ZTE arises from two coupled mechanisms. First, magnetic ordering in the Fe sublattice induces a 3*d* bonding state transition: depopulation of bonding states in the minority spin channel and population of nonbonding states in the majority spin channel weaken Fe—Fe bonds, generating lattice expansion stress that manifests as NTE (Figure 11c). The

© 2025 Wiley-VCH GmbH

15272648, 0, Downloaded from https://advanced.onlinelibrary.wiley.com/doi/10.1002/adem.202500833 by Technical University Delft, Wiley Online Library on [09/09/2025]. See the Terms and Conditions (https://onlinelibrary.wiley.com/terms-and-conditions) on Wiley Online Library for rules of use; OA articles are governed by the applicable Creative Commons License

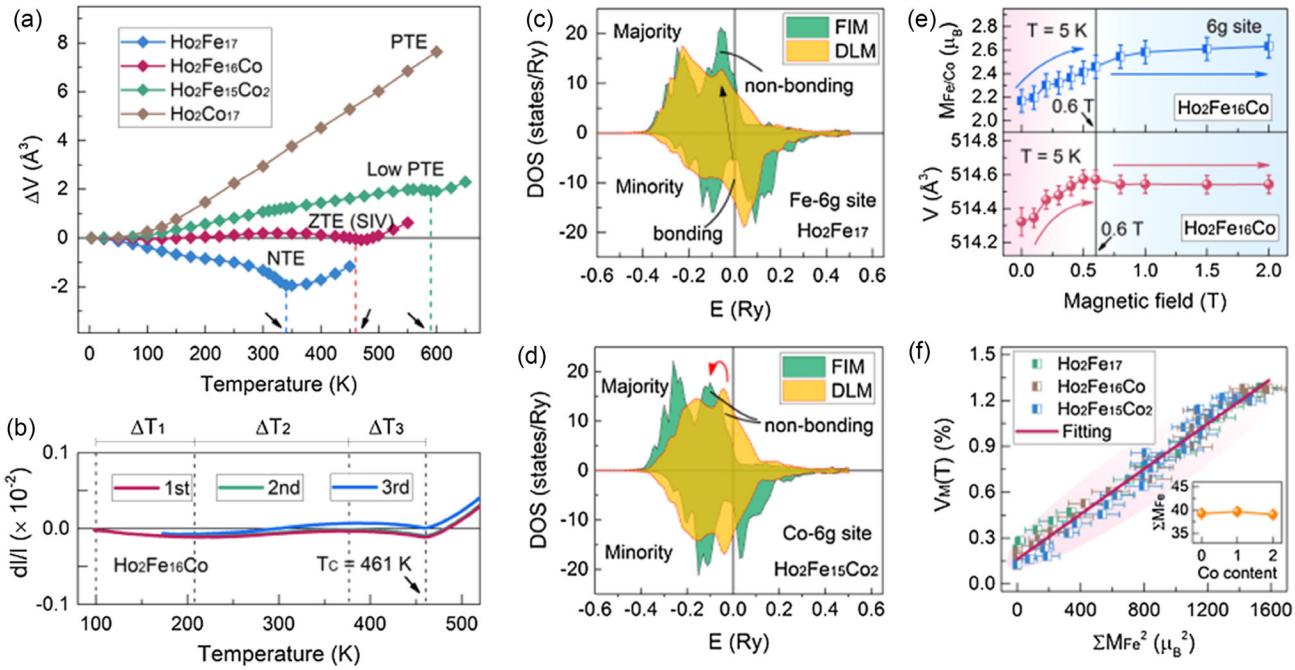

Figure 11. a) Temperature dependence of relative unit-cell volume determined by NPD refinements from 3 to 650 K for $Ho_2(Fe, Co)_{17}$ compounds; b) apparent ZTE of $Ho_2Fe_{16}Co$ compound determined by thermal dilatometer from 100 to 520 K. c) DOS of Fe atoms at 6*g* site for Ho_2Fe_{17} compound; d) Atomic resolved contribution to the DOS of Co atoms at 6*g* sites for $Ho_2Fe_{15}Co_2$ compound; e) magnetic moments of Fe/Co atoms ($M_{Fe/Co}$) at 6*g* site and unit-cell volume as a function of applied magnetic field for $Ho_2Fe_{16}Co$ compound at 5 K; f) Positive correlation between the magnetic moments of Fe sublattice ($|\Sigma M_{Fe}|$) and the contribution of magnetic ordering to the unit-cell volume. The inset shows the $|\Sigma M_{Fe}|$ as a function of Co content. Reproduced with permission.[63] Copyright 2021, American Physical Society.

magnitude of this NTE scales with the Fe magnetic moment (Figure 11f). Second, Co substitution enhances the molecular field, extending magnetic order to higher temperatures and thus widening the ZTE range. Importantly, Co introduces minimal lattice stress due to compensating changes within non-bonding electronic states (Figure 11d), enabling it to stabilize the crystal structure while synergistically balancing the NTE (from Fe sublattice magnetism) and intrinsic PTE (from lattice vibrations).

3.4. Thermal Conductivity, Electric Conductivity, and Mechanical Properties

Table 2 summarizes the physical properties of key NTE or ZTE alloys. $Fe_2Hf_{0.87}Ta_{0.13}Cu_{1.25}$, $LaFe_{54}Co_{3.5}Si_{3.35}$, and $Er_2Fe_{14}B_{1.035}$ each feature multiple phases that exhibit an exceptionally high compressive strength (CS > 1 GPa), surpassing Invar alloys. La–Fe–Co–Si alloys, however, have a much lower electrical conductivity (0.62 MSm^{-1}) than Invar, though Cu doping enhances their mechanical reliability. Fe_2(Hf, Ta)-based Laves phase alloys combine a high Young's modulus, compressive strength, and Vickers hardness with superior thermal and electrical conductivity, outperforming other metallic NTE materials. Additionally, the Fe_2Zr-based Laves phase demonstrates the widest NTE temperature range, as shown in Table 1, along with an exceptional corrosion resistance, broadening their potential for practical applications. For rare-earth-based transition metal alloys, the small CS and plasticity restrict their practical applications despite the wide ZTE window.

Table 2. Thermal conductivity (*k*, $Wm^{-1}K^{-1}$), electrical conductivity (σ, MSm^{-1}), Young's modulus (*E*, GPa), Compressive strength (*CS*, GPa), Vickers hardness (H_V), and plasticity (%) of metallic ZTE/NTE materials.

Compounds	*k*	σ	*E*	*CS*	H_V	plasticity
Invar 36[74]	10.4	1.19	141	0.282	150–200	30
$Hf_{0.87}Ta_{0.13}Fe_2$[25]	10.1	1.08	223	0.382	882	16.8
$Fe_2Hf_{0.87}Ta_{0.13}Cu_{1.25}$[67]	23.4	–	–	1.04	–	9
$LaFe_{10.5}Co_{1.0}Si_{1.5}$[52,75]	6	0.62	130	–	–	–
$LaFe_{54}Co_{3.5}Si_{3.35}$[54]	–	–		1.11	–	30.9
$(LaFe_{10.8}CoSi_{1.2})_{55}Cu_{45}$[55]	–	–	–	0.645	–	4.4
$LaFe_{11}Si_2H_x$[53]	–	–	–	0.06	–	1
$LaFe_{20.2}Co_{1.2}Si_{1.6}$[76]	–	–		1	–	3.87
$ErCo_{2.8}Fe_{0.2}$[60]	–	–	–	–	532.6	–
$Er_2Fe_{14}B_{1.35}$[61]	–	–	61.47	1.44	–	–
$Ho_2Fe_{16}Co$[63]	–	–	–	0.049	–	2
$Ho_2Fe_{16}Cr$[72]	–	–	–	0.05	–	2
$Ho_{0.04}Fe_{0.96}$[62]	–	–	–	0.88	–	15.6
$TbCo_{1.9}Fe_{0.1}$[28]	–	–	–	0.26	–	1.5

© 2025 Wiley-VCH GmbH

15272648, 0, Downloaded from https://advanced.onlinelibrary.wiley.com/doi/10.1002/adem.202500833 by Technical University Delft, Wiley Online Library on [09/09/2025]. See the Terms and Conditions (https://onlinelibrary.wiley.com/terms-and-conditions) on Wiley Online Library for rules of use; OA articles are governed by the applicable Creative Commons License

4. Correlation between MCE and ZTE

For certain Fe-based Laves phase materials, such as Fe_2(Hf, Ta), which undergo a FM to AFM transition, the FM state possesses a larger volume than the AFM state, leading to a net negative contribution to the thermal expansion. Similarly, in La(Fe, Si)$_{13}$-based compounds exhibiting a FM-to-PM transition, the loss of long-range magnetic order upon heating results in a volume contraction and induces NTE. In rare-earth-based alloys like $TbCo_{1.9}Fe_{0.1}$, the FIM-to-PM transition can lead to either NTE or ZTE, depending on the rate of decrease in the Tb magnetic moment—rapid suppression leads to NTE, while a gradual reduction results in ZTE.

The identical trends of $d\omega_s/dT$ and dM/dT as shown in **Figure** 4f, 5c, 11f, and **12**d confirm the presence of strong magneto-lattice coupling in Fe-based Laves phase and rare-earth-based alloys. According to Equation (5), the linear correlation between the ω_s and M^2 highlights the dominant role of magnetic coupling and magnetoelastic transition in driving the NTE.[27,30,38] The trend in ω_s and M^2 is nearly identical and exhibits a strong linear dependency, indicating that magnetoelastic transition dominates the NTE of Fe-based Laves phase and $Ho_2Fe_{15}Co_2$. The volume contraction is associated with the reduction in magnetic moments due to MVE counteracts the lattice expansion caused by thermal vibrations.[47] Furthermore, the constant kC from Equation (5), which quantifies the strength of this interaction, can be derived from the slope of the linear ω_s and M^2 relationship.[38] A larger kC implies a stronger magnetoelastic coupling, offering enhanced tunability of NTE through magnetic transitions. The kC values for $Fe_2Hf_{0.83}Ta_{0.17}$ and La$(Fe_{0.86}Al_{0.24})_{13}$ are 1.32×10^{-10} cm^2 A^{-2} and 1.79×10^{-10} cm^2 A^{-2}, respectively, and both are potential MCE materials with strong magnetoelastic coupling.[38]

Magnetic transitions, whether of the order-order (FM-AFM, FIM-PM) or order–disorder (FM-PM) type, play a central role in governing thermal expansion behavior in magnetic materials. Based on the underlying mechanisms of magneto-lattice coupling, strategies for achieving ZTE or NTE in magnetic systems can be broadly categorized into three approaches: 1) Chemical broadening or suppression of magnetic transitions: By chemically tuning the magnetic transition, it is possible to broaden or suppress the sharpness of the magnetoelastic transition, which reduces the abruptness of volume change and leads to ZTE. Representative systems include $(Zr_{1-x}Nb_x)Fe_2$,[64] R_2(Fe, Co)$_{17}$,[63] $Sc_{0.55}Ti_{0.45}Fe_2$,[43] $TbCo_{2-x}Fe_x$,[28] $ErCo_{2.8}Fe_{0.2}$,[65] and $LaFe_{13-x}Al_x$.[56] Further refinements can be realized through phase separation via elemental substitution,[51] phase coexistence induced by atomic vacancies,[39] or variations in sample preparation methods.[38] 2) The second approach is based on exploiting sharp magnetic transitions, below which ZTE behavior emerges due to enhanced magnetoelastic coupling. This has been observed in compounds such as $Fe_2Hf_{0.85}Ta_{0.15}C_{0.01}$,[27] La(Fe, Si)$_{13}$ hydrides,[53] and the $Mn_{1-x}Ni_xCoSi$ system.[66] 3) Introduction of secondary phases: Secondary phase formation can alter magnetoelastic interactions and fine-tune the thermal expansion response. This approach has been successfully applied in systems including $Hf_{0.9}Ta_{0.1}Fe_{2-x}X_x$ (X = Al, Co, V, Cr),[51] $Zr_{1-x}Nb_xFe_2Co_y$,[49] Ho_xFe_{1-x},[62] Fe_{2+x}(Hf, Ta),[48,67] $Hf_{0.87}Ta_{0.13}Fe_2Cu_x$,[68] $Fe_{2+x}Hf_{0.80}Nb_{0.20}$,[39] $(LaFe_{10.8}CoSi_{1.2})_{(100-y)}Cu_y$,[55] $LaFe_{54}Co_{3.5}Si_{3.35}$.[54]

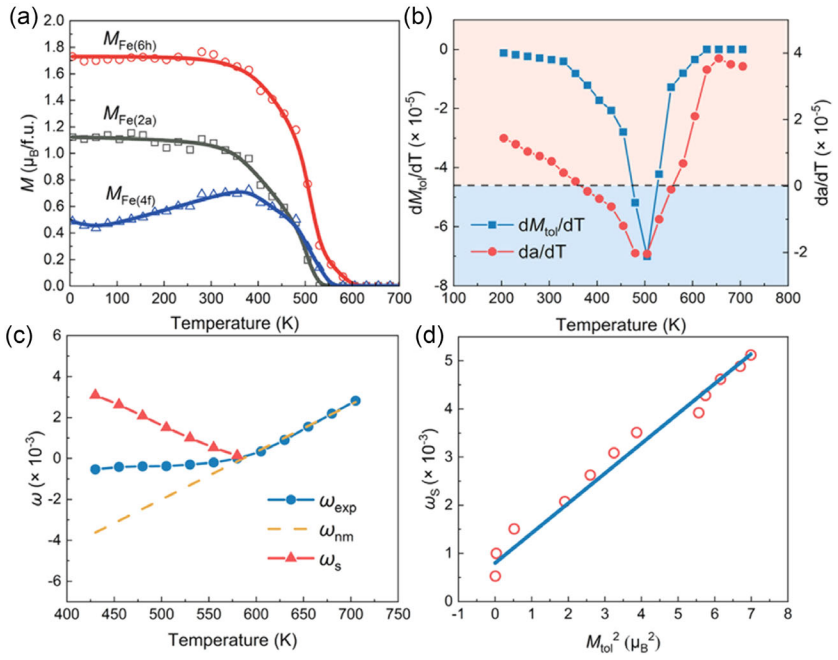

Figure 12. a) Temperature dependence of the magnetic moment at three different Fe sites. b) Rate of change of total moment dM_{tol}/dT vs da/dT for $HfFe_{2.5}$. c) Thermal expansion characteristics of $HfFe_{2.5}$. d) Correlation between M_{tol}^2 and ω_S for ZTE in $HfFe_{2.5}$. Reproduced with permission.[47]. Copyright 2022, American Chemical Society.

© 2025 Wiley-VCH GmbH

15272648, 0, Downloaded from https://advanced.onlinelibrary.wiley.com/doi/10.1002/adem.202500833 by Technical University Delft, Wiley Online Library on [09/09/2025]. See the Terms and Conditions (https://onlinelibrary.wiley.com/terms-and-conditions) on Wiley Online Library for rules of use; OA articles are governed by the applicable Creative Commons License

5. Summary and Outlook

This review examines the ZTE in MCE materials, focusing on representative systems such as Fe-based Laves phases, La–Fe–Si(Al)-based alloys, and rare-earth-based compounds. The CTE and temperature window of the ZTE for representative magnetic systems are presented in **Figure 13**. The physical origins of both the NTE and MCE are rooted in lattice-spin coupling, enabling the tuning of the NTE to achieve a ZTE. An abnormal lattice expansion in giant MCE materials provides a platform for ZTE exploration. Weakening the magnetoelastic transition by chemical substitution can certainly widen the ZTE performance. However, the ZTE behavior occurring can also be attributed to an enhanced magnetoelastic coupling. Therefore, understanding the ZTE-MCE correlation is key to regulating phase transitions and discovering novel ZTE materials. Techniques such as SXRD, NPD, electron probe X-ray microanalysis, Mössbauer spectroscopy, high-resolution transmission electron microscopy, and EXAFS are instrumental in revealing the structural and magnetic features at macroscale, microscale, and atomic levels and guiding the design and stabilization of ZTE behavior.

To accelerate the discovery of novel ZTE materials, we propose three promising research directions. 1) Hybrid ZTE design: Inspired by the approach of Cao et al., establishing quantitative relationships in La(Fe, Si)$_{13}$-based alloys between constituent phases can guide the development of composite systems with tailored ZTE behavior. 2) High-throughput doping and screening: Systematic doping strategies have proven effective for tuning magnetic and structural transitions, thereby broadening the temperature window for ZTE. The integration of high-throughput experimental workflows can accelerate the identification of optimal compositions, particularly for enhancing magnetoelastic coupling and thermal expansion control. 3) Machine learning (ML)-driven discovery: Although ML has shown success in identifying promising magnetocaloric materials, its application to ZTE systems remains underexplored. By adapting existing ML models and incorporating features specific to magnetoelastic behavior, new ML frameworks can be developed to predict ZTE candidates and uncover underlying design principles, significantly accelerating material discovery.

Additionally, the low magnetic transition temperatures of most magnetic ZTE systems limit their practical applications to cryogenic or low-temperature environments. Moreover, as intermetallic compounds, these materials often exhibit high hardness and low plasticity, which hinders processing and raises concerns regarding mechanical reliability. Key functional properties such as electrical and thermal conductivity, as well as long-term mechanical stability under cyclic loading, remain insufficiently studied in many ZTE candidates. Future research should therefore prioritize the enhancement of mechanical performance, corrosion resistance, and overall durability to enable broader technological deployment.

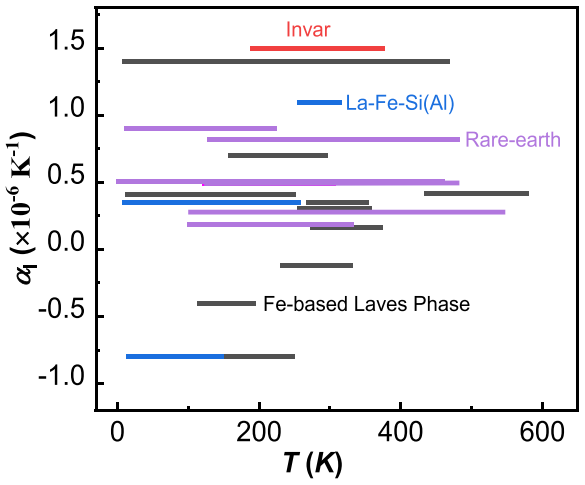

Figure 13. a) Linear CTE and temperature window of the ZTE of representative magnetic systems (data from Table 1 selected for $|\alpha_l| < 1.5 \times 10^{-6}\,K^{-1}$). Different line colors represent different types of materials systems.

Acknowledgements

This work was financially supported by the National Natural Science Foundation of China (grant no. 52401230, 52472274) and the Zhejiang Provincial Natural Science Foundation of China (grant no. ZCLMS25E0101).

Conflict of Interest

The authors declare no conflict of interest.

Author Contributions

Qi Shen: conceptualization (lead); formal analysis (equal); funding acquisition (equal); validation (lead); writing—original draft (lead); writing—review & editing (supporting). **Niels van Dijk**: formal analysis (supporting); resources (supporting); validation (supporting); visualization (supporting); writing—review & editing (equal). **Ekkes Brück**: formal analysis (equal); resources (equal); supervision (equal); validation (equal); writing—review & editing (equal). **Lingwei Li**: conceptualization (supporting); formal analysis (supporting); methodology (supporting); resources (equal); validation (equal); writing—original draft (supporting); writing—review & editing (equal).

Keywords

magnetocaloric effect, negative thermal expansion, zero thermal expansion

Received: March 26, 2025
Revised: June 22, 2025
Published online:

[1] C. E. Guillaume, *CR Acad. Sci.* **1897**, *125*, 235.
[2] M. Schilfgaarde, I. A. Abrikosov, B. Johansson, *Nature* **1999**, *400*, 46.
[3] T. Yokoyama, K. Eguchi, *Phys. Rev. Lett.* **2011**, *107*, 065901.
[4] F. Zhang, X. Miao, N. van Dijk, E. Brück, Y. Ren, *Adv. Energy Mater.* **2024**, *14*, 2400369.
[5] J. Y. Law, L. M. Moreno-Ramírez, Á. Díaz-García, V. Franco, *J. Appl. Phys.* **2023**, *133*, 040903.
[6] Y. K. Zhang, Y. Z. Na, W. X. Hao, T. Gottschall, L. W. Li, *Adv. Funct. Mater.* **2024**, *34*, 2409061.
[7] E. Brück, *J. Phys. D: Appl. Phys.* **2005**, *38*, R381.

© 2025 Wiley-VCH GmbH

15272648, 0, Downloaded from https://advanced.onlinelibrary.wiley.com/doi/10.1002/adem.202500833 by Technical University Delft, Wiley Online Library on [09/09/2025]. See the Terms and Conditions (https://onlinelibrary.wiley.com/terms-and-conditions) on Wiley Online Library for rules of use; OA articles are governed by the applicable Creative Commons License

[8] Y. Zhang, A. Li, W. Hao, H. F. Li, L. Li, *Acta Mater.* **2025**, *292*, 121033.
[9] A. Fujita, S. Fujieda, Y. Hasegawa, K. Fukamichi, *Phys. Rev. B* **2003**, *67*, 104416.
[10] F. Hu, B. Shen, J. Sun, Z. Cheng, G. Rao, X. Zhang, *Appl. Phys. Lett.* **2001**, *78*, 3675.
[11] L. Miao, X. Lu, Z. Wei, Y. Zhang, Y. Zhang, J. Liu, *Acta Mater.* **2023**, *245*, 118635.
[12] Y. Shao, B. Lu, M. Zhang, J. Liu, *Acta Mater.* **2018**, *150*, 206.
[13] E. B. O. Tegus, K. H. J. Buschow, F. R. de Boer, *Nature* **2002**, *415*, 150.
[14] N. H. Dung, Z. Q. Ou, L. Caron, L. Zhang, D. T. C. Thanh, G. A. de Wijs, R. A. de Groot, K. H. J. Buschow, E. Brück, *Adv. Energy Mater.* **2011**, *1*, 1215.
[15] F. Zhang, P. Feng, A. Kiecana, Z. Wu, Z. Bai, W. Li, H. Chen, W. Yin, X. W. Yan, F. Ma, N.v. Dijk, E. Brück, Y. Ren, *Adv. Func. Mater.* **2024**, *34*, 2409270.
[16] Y. K. Zhang, Y. Na, X. Zhao, Y. Xie, *J. Mater. Chem. A* **2025**, *13*, 19923.
[17] X. Tang, H. Sepehri-Amin, N. Terada, A. Martin-Cid, I. Kurniawan, S. Kobayashi, Y. Kotani, H. Takeya, J. Lai, Y. Matsushita, T. Ohkubo, Y. Miura, T. Nakamura, K. Hono, *Nat. Commun.* **2022**, *13*, 1817.
[18] F. Chen, J. Xu, X. Zhao, Y. Na, Y. Zhang, *Sci. China Mater.* **2025**, *68*, 2828.
[19] W. Liu, T. Gottschall, F. Scheibel, E. Bykov, A. Aubert, N. Fortunato, B. Beckmann, A. M. Döring, H. Zhang, K. Skokov, O. Gutfleisch, *J. Alloys Compd.* **2024**, *995*, 174612.
[20] W. Chen, J. L. Lin, X. Wang, L. W. Li, *J. Magn. Magn. Mater.* **2025**, *626*, 173107.
[21] F. Guillou, H. Yibole, N. H. van Dijk, E. Brück, *J. Alloys Compd.* **2015**, *632*, 717.
[22] F. Pressacco, V. Uhliotar, M. Gatti, A. Bendounan, E. E. Fullerton, F. Sirotti, *Sci. Rep.* **2016**, *6*, 22383.
[23] J. B. L. Morellon, P. A. Algarabel, M. R. Ibarra, *Phys. Rev. B* **2000**, *62*, 1022.
[24] B. G. Shen, J. R. Sun, F. X. Hu, H. W. Zhang, Z. H. Cheng, *Adv. Mater.* **2009**, *21*, 4545.
[25] L. F. Li, P. Tong, Y. M. Zou, W. Tong, W. B. Jiang, Y. Jiang, X. K. Zhang, J. C. Lin, M. Wang, C. Yang, X. B. Zhu, W. H. Song, Y. P. Sun, *Acta Mater.* **2018**, *161*, 258.
[26] J. Chen, L. Hu, J. Deng, X. Xing, *Chem. Soc. Rev.* **2015**, *44*, 3522.
[27] J. Xu, Z. Wang, H. Huang, Z. Li, X. Chi, D. Wang, J. Zhang, X. Zheng, J. Shen, W. Zhou, Y. Gao, J. Cai, T. Zhao, S. Wang, Y. Zhang, B. Shen, *Adv. Mater.* **2023**, *35*, 2208635.
[28] Y. Song, J. Chen, X. Liu, C. Wang, J. Zhang, H. Liu, H. Zhu, L. Hu, K. Lin, S. Zhang, X. Xing, *J. Am. Chem. Soc.* **2018**, *140*, 602.
[29] E. Liang, Q. Sun, H. Yuan, J. Wang, G. Zeng, Q. Gao, *Front. Phys.* **2021**, *16*, 53302.
[30] Y. Song, N. Shi, S. Deng, X. Xing, J. Chen, *Prog. Mater. Sci.* **2021**, *121*, 100835.
[31] L. V. B. Diop, O. Isnard, E. Suard, D. Benea, *Solid State Commun.* **2016**, *229*, 16.
[32] L. V. B. Diop, J. Kastil, O. Isnard, Z. Arnold, J. Kamarad, *J. Alloys Compd.* **2015**, *627*, 446.
[33] L. V. B. Diop, O. Isnard, M. Amara, F. Gay, J. P. Itié, *J. Alloys Compd.* **2020**, *845*, 156310.
[34] Z. Song, Z. Li, B. Yang, H. Yan, C. Esling, X. Zhao, L. Zuo, *Materials* **2021**, *14*, 1.
[35] S. Y. Dong, X. Z. Yang, J. Y. Chen, Q. Shao, B. Qian, Z. D. Han, C. L. Zhang, X. F. Jiang, *Physica B* **2015**, *466–467*, 86.
[36] J. Sheng, J. Xu, L. Xi, S. Xing, S. Li, X. Kan, X. Zheng, H. Huang, L. Wang, Y. Han, S. Zhou, B. Shen, S. Wang, *Appl. Phys. Lett.* **2025**, *126*, 032404.
[37] J. Dong, M. Zhang, J. Liu, P. Zhang, A. Yan, *Physica B* **2015**, *476*, 171.
[38] Q. Shen, I. Batashev, F. Zhang, H. Ojiyed, I. Dugulan, N. van Dijk, E. Brück, *Acta Mater.* **2023**, *257*, 119149.
[39] Q. Shen, Z. Zhang, C. de Vries, A. I. Dugulan, N. van Dijk, E. Brück, L. Li, *Chem. Mater.* **2024**, *36*, 6299.
[40] Y. Song, M. Xu, X. Zheng, C. Zhou, N. Shi, Q. Huang, S. Wang, Y. Jiang, X. Xing, J. Chen, *J. Mater. Sci. Technol.* **2023**, *147*, 102.
[41] Q. Shen, F. Zhang, I. Dugulan, N. van Dijk, E. Brück, *Scr. Mater.* **2023**, *232*, 115482.
[42] H. Yibole, A. K. Pathak, Y. Mudryk, F. Guillou, N. Zarkevich, S. Gupta, V. Balema, V. K. Pecharsky, *Acta Mater.* **2018**, *154*, 365.
[43] Y. Song, Q. Sun, M. Xu, J. Zhang, Y. Hao, Y. Qiao, S. Zhang, Q. Huang, X. Xing, J. Chen, *Mater. Horiz.* **2020**, *7*, 275.
[44] M. Xu, Q. Li, Y. Song, Y. Xu, A. Sanson, N. Shi, N. Wang, Q. Sun, C. Wang, X. Chen, Y. Qiao, F. Long, H. Liu, Q. Zhang, A. Venier, Y. Ren, F. d'Acapito, L. Olivi, D. O. De Souza, X. Xing, J. Chen, *Nat. Commu.* **2023**, *14*, 4439.
[45] Y. Cao, Y. Xu, S. Khmelevskyi, M. Avdeev, C.-W. Wang, S. Hu, K. Ohara, Y. Xia, X. Chen, Q. Li, J. Deng, J. Miao, K. Lin, X. Xing, *Chem. Mater.* **2023**, *35*, 9167.
[46] Y. Sun, Y. Cao, S. Hu, M. Avdeev, C.-W. Wang, S. Khmelevskyi, Y. Ren, S. H. Lapidus, X. Chen, Q. Li, J. Deng, J. Miao, K. Lin, X. Kuang, X. Xing, *J. Am. Chem. Soc.* **2023**, *145*, 17096.
[47] M. Xu, Y. Song, Y. Xu, Q. Sun, F. Long, N. Shi, Y. Qiao, C. Zhou, Y. Ren, J. Chen, *Chem. Mater.* **2022**, *34*, 9437.
[48] D. Cen, B. Wang, R. Chu, Y. Gong, G. Xu, F. Chen, F. Xu, *Scr. Mater.* **2020**, *186*, 331.
[49] R. Y. Yanming Sun, S. Khmelevskyi, K. Kato, Y. Cao, S. Hu, M. Avdeev, C.-W. Wang, C. Yu, Q. Li, K. Lin, X. Kuang, X. Xing, *Nat. Sci. Rev.* **2025**, *12*.
[50] W. Li, K. Lin, Y. Yan, C. Yu, Y. Cao, X. Chen, C. W. Wang, K. Kato, Y. Chen, K. An, Q. Zhang, L. Gu, Q. Li, J. Deng, X. Xing, *Adv. Mater.* **2022**, *34*, 2109592.
[51] H. Wang, Y. H. Wang, Y. Y. Gong, G. Z. Xu, E. Liu, X. F. Miao, Y. J. Zhang, Y. Y. Shao, J. Liu, N. Ui Hassan, I. A. Shah, F. Xu, *Rare Metals* **2024**, *43*, 6596.
[52] R. Huang, Y. Liu, W. Fan, J. Tan, F. Xiao, L. Qian, L. Li, *J. Am. Chem. Soc.* **2013**, *135*, 11469.
[53] S. Li, R. Huang, Y. Zhao, W. Wang, Y. Han, L. Li, *Adv. Func. Mater.* **2016**, *27*, 1604195.
[54] C. Yu, K. Lin, Q. Zhang, H. Zhu, K. An, Y. Chen, D. Yu, T. Li, X. Fu, Q. Yu, L. You, X. Kuang, Y. Cao, Q. Li, J. Deng, X. Xing, *Nat. Commu.* **2024**, *15*, 2252.
[55] Y. Liu, J. Li, Y. Qian, S. Qie, S. Mi, Z. Xu, H. Xie, X. Song, T. Ma, *Acta Mater.* **2024**, *275*, 120058.
[56] W. Li, R. Huang, W. Wang, Y. Zhao, S. Li, C. Huang, L. Li, *Phys. Chem. Chem. Phys.* **2015**, *17*, 5556.
[57] Y. Song, R. Huang, Y. Liu, Z. Zhang, Q. Huang, Y. Jiang, S. Wang, L. Li, X. Xing, J. Chen, *Chem. Mater.* **2020**, *32*, 7535.
[58] L. Li, M. Yan, *J. Alloys Compd.* **2020**, *823*, 153810.
[59] M. Halder, S. M. Yusuf, M. D. Mukadam, K. Shashikala, *Phys. Rev. B* **2010**, *81*, 174402.
[60] J. Xu, G. Wang, S. Xing, L. Xi, J. Sheng, S. Li, X. Kan, M. Zheng, Y. Gao, D. Wang, X. Zheng, J. Zhang, J. Xu, W. Yin, S. Zhou, B. Shen, S. Wang, *Mater.* **2024**, *35*, 2416314.
[61] C. Yu, K. Lin, X. Chen, S. Jiang, Y. Cao, W. Li, L. Chen, K. An, Y. Chen, D. Yu, K. Kato, Q. Zhang, L. Gu, L. You, X. Kuang, H. Wu, Q. Li, J. Deng, X. Xing, *Nat. Commun.* **2023**, *14*, 3135.
[62] C. Yu, K. Lin, S. Jiang, Y. Cao, W. Li, Y. Wang, Y. Chen, K. An, L. You, K. Kato, Q. Li, J. Chen, J. Deng, X. Xing, *Nat. Commu.* **2021**, *12*, 4701.
[63] Y. Cao, K. Lin, S. Khmelevskyi, M. Avdeev, K. M. Taddei, Q. Zhang, Q. Huang, Q. Li, K. Kato, C. C. Tang, A. Gibbs, C.-W. Wang, J. Deng, J. Chen, H. Zhang, X. Xing, *Phys. Rev. Lett.* **2021**, *127*, 055501.
[64] Y. Song, Q. Sun, T. Yokoyama, H. Zhu, Q. Li, R. Huang, Y. Ren, Q. Huang, X. Xing, J. Chen, *J. Phys. Chem. Lett.* **2020**, *11*, 1954.

 © 2025 Wiley-VCH GmbH

15272648, 0, Downloaded from https://advanced.onlinelibrary.wiley.com/doi/10.1002/adem.202500833 by Technical University Delft, Wiley Online Library on [09/09/2025]. See the Terms and Conditions (https://onlinelibrary.wiley.com/terms-and-conditions) on Wiley Online Library for rules of use; OA articles are governed by the applicable Creative Commons License

[65] Y. Qiao, Y. Song, M. Xu, Q. Gao, Y. Ren, X. Xing, J. Chen, *Inorg. Chem. Front.* **2019**, *6*, 3225.
[66] J. Liu, B. Ding, Y. Yao, X. Xi, Z. Cheng, J. Wang, C.-w. Wang, G. Wu, W. Wang, *NPG Asia Mater.* **2021**, *13*, 70.
[67] L. Li, P. Tong, W. Tong, W. Jiang, Y. Ding, H. Lin, J. Lin, C. Yang, F. Zhu, X. Zhang, X. Zhu, W. Song, Y. Sun, *Inorg. Chem.* **2019**, *58*, 16818.
[68] L. F. Li, P. Tong, W. B. Jiang, J. C. Lin, F. Zhu, M. F. Shu, Z. T. Fang, G. C. Zhao, Z. Z. Jiang, W. Wang, C. B. Pan, X. B. Zhu, W. H. Song, Y. P. Sun, *Materialia* **2020** *9*, 100637.
[69] Q. Shen, Tuning Magnetoelastic Transitions in Mn2Sb-based and Fe2Hf-based Magnetocaloric Materials, *Ph.D. Thesis*, Delft University of Technology **2023**.
[70] W. Wang, R. Huang, W. Li, J. Tan, Y. Zhao, S. Li, C. Huang, L. Li, *Phys. Chem. Chem. Phys.* **2015**, *17*, 2352.
[71] Y. Song, J. Chen, X. Liu, C. Wang, Q. Gao, Q. Li, L. Hu, J. Zhang, S. Zhang, X. Xing, *Chem. Mater.* **2017**, *29*, 7078.
[72] S. Dan, S. Mukherjee, C. Mazumdar, R. Ranganathan, *RSC Adv.* **2016**, *6*, 94809.
[73] Y. N. Masayuki Shiga, *J. Phys. Soc. Jpn.* **1979**, *47*, 1446.
[74] W. Martienssen, H. Warlimont, *Springer Handbook of Condensed Matter and Materials Data*, Springer, New York **2005**, p. 783.
[75] B. Kaeswurm, A. Barcza, M. Vögler, P. T. Geiger, M. Katter, O. Gutfleisch, L. F. Cohen, *J. Alloys Compd.* **2017**, *697*, 427.
[76] J. Wang, J. Liu, X. Miao, G. Xu, F. Chen, Q. Zhang, F. Xu, *J. Alloys Compd.* **2018**, *769*, 233.

Qi Shen is currently an associate researcher at Hangzhou Dianzi University. She received his BS in Materials Science and Technology from Wuhan University of Technology, China, in 2016, and obtained her Ph.D. in Applied Science from Delft University of Technology, the Netherland, in 2023. Her current research interests include negative/zero thermal expansion, magnetocaloric effect and orrelated physical or chemical properties in energy materials.

© 2025 Wiley-VCH GmbH

15272648, 0, Downloaded from https://advanced.onlinelibrary.wiley.com/doi/10.1002/adem.202500833 by Technical University Delft, Wiley Online Library on [09/09/2025]. See the Terms and Conditions (https://onlinelibrary.wiley.com/terms-and-conditions) on Wiley Online Library for rules of use; OA articles are governed by the applicable Creative Commons License